TUDelft

Delft University of Technology

Integration of solid oxide fuel cell and internal combustion engine for maritime applications

Sapra, Harsh; Stam, Jelle; Reurings, Jeroen; van Biert, Lindert; van Sluijs, Wim; de Vos, Peter; Visser, Klaas; Vellayani, Aravind Purushothaman; Hopman, Hans
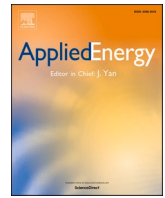
Important note
To cite this publication, please use the final published version (if applicable).
Please check the document version above.

Integration of solid oxide fuel cell and internal combustion engine for maritime applications

Harsh Sapra [a,*], Jelle Stam [b], Jeroen Reurings [c], Lindert van Biert [a], Wim van Sluijs [d],
Peter de Vos [a], Klaas Visser [a], Aravind Purushothaman Vellayani [b], Hans Hopman [a]

[a] *Department of Maritime & Transport Technology, Delft University of Technology, Mekelweg 2, Delft 2628 CD, the Netherlands*
[b] *Department of Process & Energy, Delft University of Technology, Mekelweg 2, Delft 2628 CD, the Netherlands*
[c] *Defence Materiel Organisation, Maritime Systems, Ministry of Defence, Utrecht 3584 AB, the Netherlands*
[d] *Pon Power Nederland, Ketelweg 20, Papendrecht 3356 LE, the Netherlands*

HIGHLIGHTS

- A novel SOFC-ICE integration approach for power generation onboard ships.
- Significant efficiency and emission improvements over traditional marine engines.
- The SOFC took 600 seconds and the ICE took 14 seconds for the same load change.
- SOFC-ICE power split favouring the ICE is beneficial for maritime applications.

ARTICLE INFO

ABSTRACT

The current literature on solid oxide fuel cell and internal combustion engine (SOFC-ICE) integration is focused on the application of advanced combustion technologies operating as bottoming cycles to generate a small load share. This integration approach can pose challenges for ships such as restricted dynamic capabilities and large space and weight requirements. Furthermore, the potential of SOFC-ICE integration for marine power generation has not been explored. Consequently, the current work proposes a novel approach of SOFC-ICE integration for maritime applications, which allows for high-efficiency power generation while the SOFC anode-off gas (AOG) is blended with natural gas (NG) and combusted in a marine spark-ignited (SI) engine for combined power generation. The objective of this paper is to investigate the potential of the proposed SOFC-ICE integration approach with respect to system efficiency, emissions, load sharing, space and weight considerations and load response. In this work, a verified zero-dimensional (0-D) SOFC model, engine experiments and a validated AOG-NG mean value engine model is used. The study found that the SOFC-ICE integration, with a 67–33 power split at 750 kWe power output, yielded the highest efficiency improvement of 8.3% over a conventional marine natural gas engine. Simulation results showed that promising improvements in efficiency of 5.2%, UHC and NOx reductions of about 30% and CO_2 reductions of about 12% can be achieved from a 33–67 SOFC-ICE power split with comparatively much smaller increments in size and weight of 1.7 times. Furthermore, the study concluded that in the proposed SOFC-ICE system for maritime applications, a power split that favours the ICE would significantly improve the dynamic capabilities of the combined system and that the possible sudden and large load changes can be met by the ICE.

1. Introduction

Technological advancements over the past decades have helped reduce ship emissions and fuel consumption of the traditional diesel marine engines [1,2]. However, the Tier-III NOx emission limits set up by the International Maritime Organization cannot be met by upgrading the diesel engines alone [3,4]. Therefore, with the advent of strict emission regulations, the maritime industry is transitioning to cleaner and alternative fuels. The choice of future maritime fuel is dictated by

Nomenclature

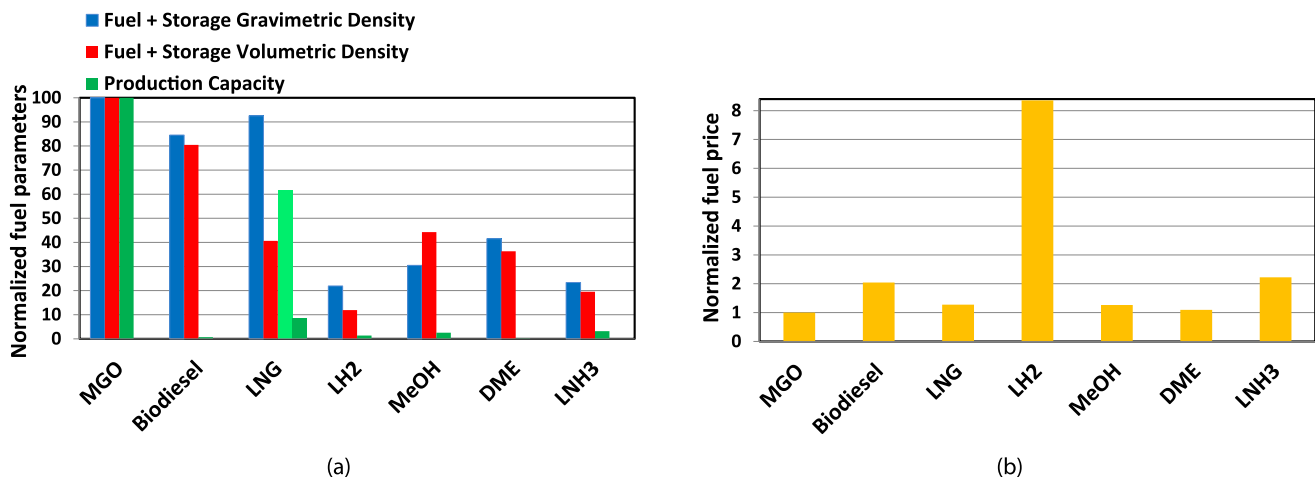|	
SOFC	Solid oxide fuel cell
ICE	Internal combustion engine
MGO	Marine gas oil
LNG	Liquified natural gas
LH2	Liquified hydrogen
MeOH	Methanol
DME	Dimethyl ether
LNH3	Liquid ammonia
GT	Gas turbine
ST	Steam turbine
HCCI	Homogenous charge compression ignition
RCCI	Reactivity controlled compression ignition
SAI	Spark-assisted ignition
AOG-NG	Anode-off gas-natural gas
ONG	Only natural gas
0-D	Zero-dimensional
MVEM	Mean value engine model
HRR	Heat release rate
MSR	Methane steam reforming
WGS	Water–gas shift
S/C	Steam-to-carbon
HOR	Hydrogen oxidation reaction
PEN	Positive electrode, electrolyte, negative electrode
PoD	Power density
i-V	Current–voltage
H_2-NG	Hydrogen-natural gas blend
CO_2-NG	Carbon dioxide-natural gas blend
H_2-CO_2-NG	Hydrogen-carbon dioxide-natural gas blend
UHC	Unburnt hydrocarbon
NOx	Nitrogen oxides
MAP	Manifold pressure
I-ICE	Integrated-internal combustion engine
EC	Energy contribution
LHV	Lower heating value
P.H.	Preheater
C.O.	Cooler
S.H.	Superheater
Evap	Evaporator
Eco	Economiser
PS	Power-split
PRR	Pre-reformer ratio

Fig. 1. Relative comparison of estimated energy densities, production capacity (a) and price (b) of alternative maritime fuels. Calculations based on LHV, storage from [5–10], production capacity from [11–15] and fuel costs from [16–21]. The production capacities are calculated in Million Metric Tons (MMT), Gravimetric energy density in MJ kg^{-1}, volumetric energy density in MJ L^{-1} and fuel costs in US \$ MJ^{-1} of energy available from fuel. The light green bar in (a) signifies the production capacity of natural gas (NG) while the dark green bar signifies the global liquefication capacity of NG.

various parameters such as fuel cost, availability, infrastructure, safety, environmental impact and technical feasibility. Fig. 1 compares the energy densities (including storage), current availability and cost estimates of prospective maritime fuels relative to marine gas oil (diesel fuel). The fuel costs are calculated in US \$ MJ^{-1} of energy available from fuel. The energy densities provided in Fig. 1 include the weight and volume of the storage system. The production capacities of different fuels presented in Fig. 1 are based on values found for the period of 2018–2019. At the same time, the fuel costs are calculated based on data available for the period of 2019–2020.

As seen from Fig. 1, at present, natural gas is the only competitive alternative to diesel with significant advantages over other alternative maritime fuels such as highest production capacity, expanding infrastructure, lower costs, highest gravimetric energy density, non-toxicity, high technical feasibility in engines and fuel cells, reduction in carbon dioxide (CO_2) emissions and large reductions in emissions of sulphur

oxides (SOx), nitrogen oxides (NOx) and particulate matter [5,22]. Armed with conclusive advantages over other alternative fuels, natural gas is poised to transition into a global maritime fuel. Fuelled by this motivation, this paper explores the potential of a natural gas (NG)-fuelled combined solid oxide fuel cell (SOFC) and internal combustion engine (ICE)-based power generation system for maritime applications. In this paper, the authors propose, for large ocean-going ships, a novel marine power generation concept, which employs the SOFC to provide electrical power, and the anode-off gas (gas at fuel cell exhaust) is used in a marine spark-ignited (SI) NG engine to deliver additional electrical power as part of the electrical power plant architecture. The SOFC anode-off gas is a mixture of hydrogen, carbon monoxide, carbon dioxide and water vapour.

1.1. Overview of SOFC combined cycles

In recent years, SOFCs have become the focus of numerous research investigations due to their high-efficiency, ultra-low emissions and noise-free operation [5,23]. Although a promising technology, their limited development state, low gravimetric and volumetric density and high costs have hindered their wide-spread adoption [5]. To offset these challenges and capitalize on the enhanced efficiency SOFC operation, a number of researchers have investigated SOFC combined cycles [24,25]. For instance, SOFC-Gas turbine (GT) systems have been widely studied, both computationally and experimentally [26,27]. In both SOFC-GT and SOFC-ST systems, the SOFC functions as a high-efficiency electrical power generation device while the turbines generate additional power by expanding the combusted anode-off gas or steam generated from the combustion heat. The extra power generated from turbines in SOFC combined cycles increases the electrical efficiency. Furthermore, SOFC-GT and SOFC-ST combined systems can allow for pressurised SOFC operation, which leads to further improvements in efficiency due to increased cell voltages as shown by VanBiert et al. [28]. Model simulation studies have shown that SOFC-GT systems have the potential of achieving high efficiencies ranging from 58.1% to even 67.9% for a 1.5 MW output with a pressure ratio of 7.8 [28,29]. Similarly, Park et al. [30] showed efficiencies of 59.2% and 61.6% for the ambient and pressurised SOFC-gas turbine systems, respectively. Besides simulation studies, few experimental demonstrations by industries such as Mitsubishi, Rolls Royce, General Electric and Allison Engines have been reported for such systems due to high costs and complexities [27,31] Although presented SOFC-GT systems have showcased high rated operation efficiencies, off design and part load performance have been proven to be much less efficient. An efficiency drop from 60.6% to 37.4% was reported for the part load performance at 57% load by Chan et al. [32]. Thus, the matching of SOFC and GT for full load operation can lead to poor part load performance with complex control architecture requirement due to SOFC-GT coupling [31].

Another alternative SOFC combined power generation system is the integration of SOFC with a reciprocating internal combustion engine. The better part load performance, better economics, robustness and simplified integration potential of engines compared to gas or steam turbines make engines highly suitable for integration with SOFCs. SOFCs have poor transient and start-up capabilities [5]. On the contrary, engines are known for their instant load-taking abilities, therefore, load fluctuations could be achieved by the engine in an integrated SOFC-ICE system. In the case of SOFC-GT and SOFC-ST integration, load transients can be challenging due to complex architecture and control management requirements caused by the coupling of the two systems [31,33]. A de-coupled SOFC-ICE system can meet the instant load change by bypassing the fuel directly to the engine [31]. Additionally, in a combined cycle, engines have shown superior dynamic load response compared to gas turbines while operating at higher part load efficiencies [34–36]. Internal combustion engines are also less capital intensive than their gas turbine counterparts, thus, allowing for a more economic SOFC combined cycle [37]. Moreover, system power and efficiency produced by a SOFC-ICE system will be less sensitive to ambient condition variations as engines are, in general, less sensitive to ambient conditions compared to gas turbines [31]. Therefore, an integrated SOFC-ICE system can be a promising power generation alternative.

Motivated by the above reasoning, researchers have investigated the integration of a SOFC with engines operating on different combustion strategies such as homogenous charge compression ignition (HCCI) [38,39], reactivity controlled compression ignition (RCCI) [31] and spark-assisted ignition (SAI) [40]. For SOFC-HCCI engine integration, researchers have investigated the economic feasibility based on a thermo-economic analysis [37,41]. Choi et al. demonstrated HCCI engine operation with a variety of anode-off gas compositions [42] and also researched the causes and impact of heat losses in a HCCI engine operating on SOFC anode-off gas [43]. HCCI is an advanced combustion

technology that has shown to achieve high engine efficiencies with low NOx emissions for a significantly diluted fuel charge of SOFC anode-off gas [44]. The SOFC-HCCI engine integration allows high-efficiency operation of SOFC while the SOFC anode-off gas is combusted in an HCCI engine allowing for high overall efficiency achievements [45,46]. In a relatively recent study, Choi et al. investigated the design point performance of a 5 kW SOFC-HCCI engine hybrid system with a system efficiency of 59% [47] Similarly, Wu et al. analysed a SOFC-ICE hybrid system with a metal hydride reactor and an HCCI engine to showcase high overall system efficiency improvements [48]. However, there are numerous challenges associated with HCCI operation such as difficulties in controlling auto-ignition, limited operating range, difficulties in homogeneous charge preparation and controlling knock in addition to high emissions of unburnt hydrocarbons (UHC) and carbon monoxide (CO) [49,40].

Next to HCCI combustion for SOFC-ICE integration, Chuahy et al. [31] proposed the RCCI technology, which uses the different chemical kinetic characteristics of diesel fuel and SOFC anode-off gas for improved control over the combustion start, duration and heat release compared to HCCI combustion. The authors further explained that the direct injection of diesel or liquid fuel in large percentages can allow for a rapid increase in system loading, thus, de-coupling the engine from the SOFC. Chuahy et al. used a combination of engine simulations and experiments to show an optimised SOFC-ICE combined cycle operating on diesel as the parent fuel, and capable of achieving 70% (LHV) electrical efficiency. The 70% system efficiency was achieved for a system producing approximately 1 MWe power and a load share of approximately 85%-15% between the SOFC and engine. For high system efficiency, the engine was proposed to generate a much smaller fraction of additional power from the SOFC anode-off gas. In contrast to HCCI and RCCI strategies, Kim et al. experimentally showed the feasibility of SAI combustion technology [40] for SOFC-ICE integration and explained that compression ignition (CI) may not be a practical combustion strategy for anode off-gas (with high dilution) because it requires significant compression work per chemical energy delivery. Similarly, Ran et al. experimentally investigated the combustion of SOFC anode-off gas (without water vapour) in a SI engine for additional power generation [50].

1.1.1. Maritime perspective

The above discussed SOFC combined cycles presented in the current literature employ turbine and engine bottoming cycles and are mainly focused towards distributed power generation applications. The literature on SOFC combined cycles for maritime applications is scarce [5,51]. In addition to achieving high efficiencies, power generation onboard ships poses a number of considerations, which are as follows:

- Space and weight considerations
- High dynamic loading and start-up capabilities
- Economics
- Low environmental impact
- Noise reduction

The pre-requisites of low environmental impact, noise-free operation and high power generation efficiency can be met by SOFCs. However, SOFCs are bulky, heavy and expensive with poor dynamic load response. As explained earlier, integration with engines can provide a promising opportunity to compensate for these shortcomings of SOFCs due to the superior load-taking capabilities of engines and the possibility of simplified system architecture through de-coupling. SOFC-Advanced combustion engine bottoming cycle presented in the current literature is a promising system, however, the system can pose the following challenges for maritime applications. In the existing bottoming cycle-based SOFC-ICE integration approaches, the load share of the engine was found to be around 13 to 15% [28,37,31,52]. If the engine is matched to produce the 15% load share, it lends itself to restricted dynamic
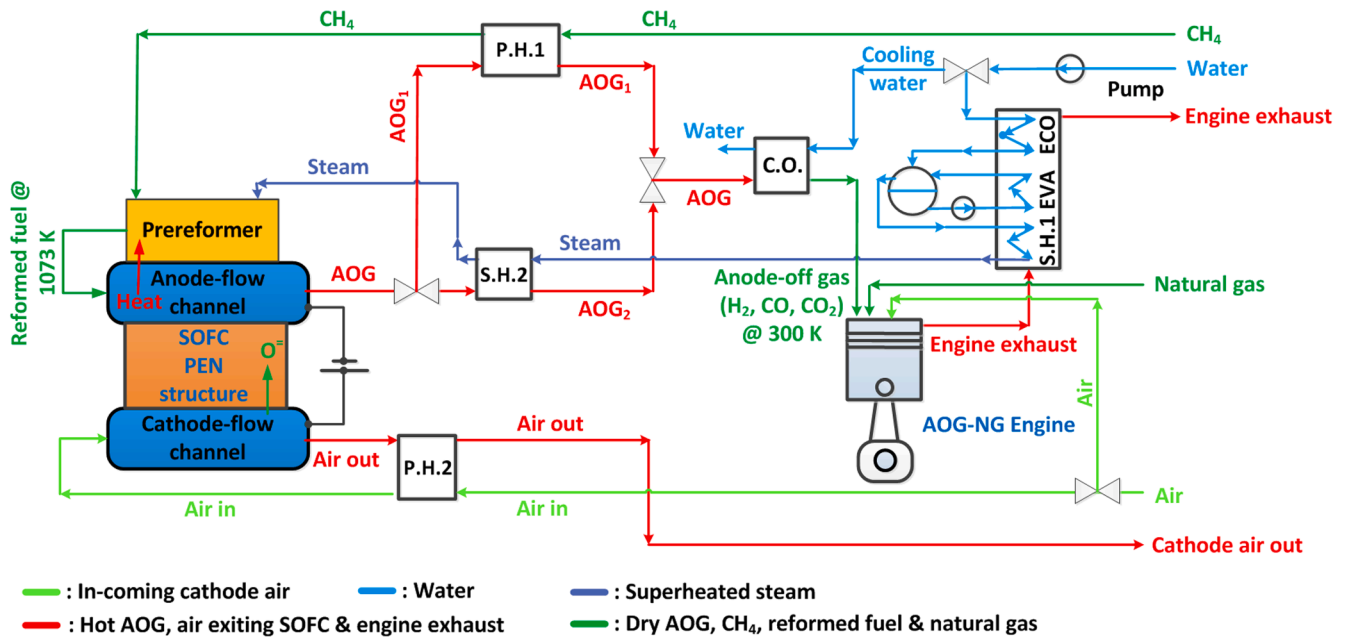
Fig. 2. System layout of the proposed SOFC-ICE integration for maritime applications. P.H.: Preheater, C.O.: Cooler, S.H. Superheater, Evap: Evaporator, Eco: Economiser.

capabilities with a possible load response of $+/-15\%$ even with instant primary fuel injection. A solution could be to integrate the SOFC with an over-capacity engine or a large battery pack for quick transients, however, such an integration would further reduce the gravimetric and volumetric density of the already heavy and large system. The power output of the integrated ICE could be increased by 25 to 50% by turbocharging, however, the small load share of the ICE in the bottoming cycle approach would still restrict the transient capabilities for maritime applications [53]. Depending on ship operations such as manoeuvring, entering a port or sailing in harsh weathers, the dynamic load changes of a ship can be large and sudden [54,55], thus, highlighting the challenge of dynamic load response associated with the existing SOFC-ICE combined cycles. The dynamic load response of the SOFC and the ICE are further discussed in Section 6.2 of this paper. In addition to ICE, smaller load shares were also found for gas and steam turbines in SOFC-GT and SOFC-ST combined cycles [36,30,51,33]. Next to the challenge of dynamic response posed by the bottoming cycle approaches in literature, HCCI and RCCI are not commercially ready engine technologies for maritime applications with a number of combined challenges such as heat release control for stable combustion, extension of operating range, high UHC and CO and low exhaust temperatures requiring high turbocharger efficiencies and improvements in after-treatment systems [56].

The above literature highlights the application of SOFC-ICE integration with advanced combustion engine technology adopted as part of a bottoming cycle to achieve high efficiencies for distributed power generation. However, there is a lack of investigations on SOFC-ICE integration for maritime applications. Furthermore, the above discussion presents the challenges of implementing a SOFC-ICE bottoming cycle for marine power generation. Consequently, the current work proposes a novel approach of SOFC-ICE integration for maritime applications, which allows for high-efficiency power generation while the varying compositions of SOFC anode-off gas are blended with natural gas and combusted in a conventional spark-ignited, lean-burn, marine engine for additional power generation. Governed by SOFC and system performance, variations in blend percentages of anode-off gas (AOG) and natural gas fuel require the integrated engine to operate on flexible anode-off gas-natural gas (AOG-NG) fuel blends for power generation rather than operating as a bottoming cycle working on only anode-off gas.

1.2. Proposed SOFC-ICE integration and research objective

Fig. 2 shows the system architecture of the proposed SOFC-ICE integration for marine power generation operating on natural gas as parent fuel. In the proposed system, the SOFC operation on natural gas (with an integrated pre-reformer) is aimed at producing high-efficiency electrical power. The reaction processes at the anode of the fuel cell lead to the production of electrons in addition to the anode-off gas, i.e., a mixture of hydrogen, carbon monoxide, carbon dioxide and water vapour. As seen from Fig. 2, the water vapour from the anode-off gas is condensed out in the cooler (C.O.). The preheaters P.H.1 and P.H.2 are used to preheat the incoming fuel and air using the outgoing cathode air and anode-off gas from the SOFC. Engine exhaust and bypassed anode-off gas are together used to superheat the steam required for SOFC operation. AOG from the SOFC contains energy in the form of hydrogen and carbon monoxide, which can be combusted in a marine natural gas engine for additional power generation, thus, enhancing efficiency and system performance through integration. The system integration approach aims at blending the SOFC AOG with natural gas to produce the engine power. However, the reactive hydrogen and high percentages of carbon dioxide in AOG can significantly impact engine performance and, thus, the SOFC-ICE integration. Therefore, to analyse the system performance, it is vital to capture the SOFC performance, its impact on anode-off gas flow and composition, and the effects of varying anode-off gas and natural gas fuel blends on SI marine engine performance. The objective of this paper is to investigate the potential and performance of the SOFC-ICE integration approach proposed for maritime applications with respect to system efficiency, emissions, load sharing, space and weight considerations and load response. This objective also represents the novelty of the paper.

This paper employs a verified SOFC cell-to-stack performance model, engine experiments and a validated anode-off gas-natural gas (AOG-NG) engine model to investigate the SOFC-ICE integration. The performance of SOFC-ICE integration is analysed at different current densities, pre-reforming ratios, fuel utilizations and power splits and compared against the performance of a conventional marine natural gas engine.
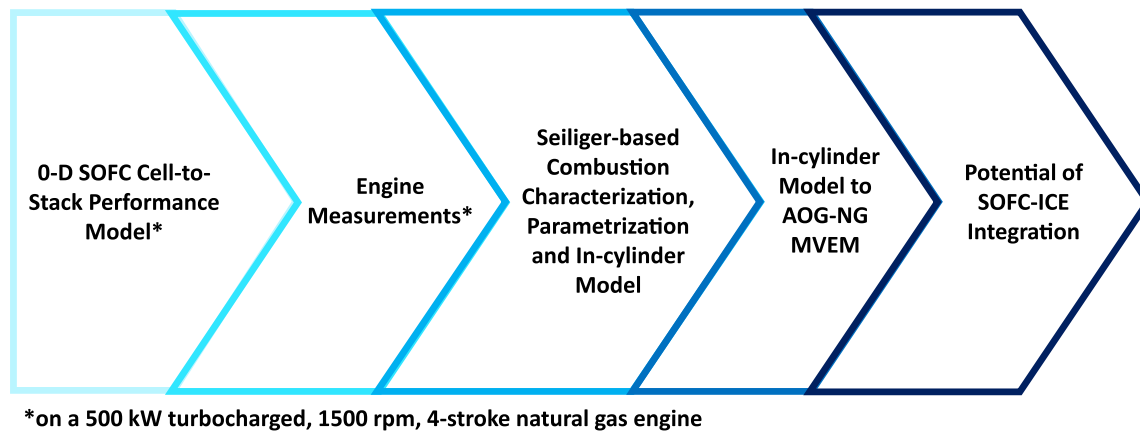
Fig. 3. Research methodology.

2. Research approach and experimental setup

2.1. Research approach

The integration of a SOFC and engine is investigated for maritime applications by combining model simulations with engine experiments. Fig. 3 shows the five-step approach employed for this research. In the first step, a 0-D SOFC cell-to-stack model was adopted to simulate the performance of the fuel cell. The SOFC model is used to capture the impact of fuel utilization on fuel cell efficiency, anode-off gas composition, flow-rates and cell temperature profiles. Fuel cell efficiency is necessary to investigate the potential of the integration. The quantity and quality of anode-off gas dictate the performance of the engine and, thus, also of the SOFC-ICE power generation system. Additionally, the determination of cell temperatures is vital to maintain and understand the required heat balance during system integration as seen in Fig. 2. The SOFC model is developed with and verified against the well-documented model by Aguiar et al. [57].

The blend of SOFC anode-off gas and natural gas is combusted in a marine NG engine to produce additional power. In the second step of this study, control and effects of combusting anode-off gas constituents blended with natural gas were studied experimentally. For this purpose, experiments were performed on a 500 kWe, eight-cylinder, turbocharged spark-ignited natural gas engine. The engine specifications can be found in a previous research paper by the authors [58] while Fig. A1 in Appendix A shows the hydrogen and carbon dioxide blending stations along with the engine test setup. As seen from Fig. 2, water vapour from the SOFC is condensed out before the anode-off gas is directed into the engine. Additionally, the effects of carbon monoxide (CO) on engine performance were not considered at this stage of the research. Section 4 provides the reasoning for the condensation of water vapour and Appendix C.1 explains the reasoning for the exclusion of CO effects. To understand and capture the effects of anode-off gas and natural gas combustion, effects of combusting only hydrogen and carbon dioxide with natural gas were first experimentally studied. Appendix A provides the details of the experimental setup and the experimentation methodology for the steady state engine measurements.

To investigate the potential of SOFC-ICE integration, simulations based on engine experiments were used to capture engine performance for conditions that could not be tested experimentally. In this step, a Seiliger cycle-based in-cylinder model was adopted to simulate the combustion and in-cylinder process for different anode-off gas and natural gas fuel blends. In the previous research paper, a Seiliger-based combustion characterization model and methodology was presented to capture the hydrogen-natural gas (H_2-NG) combustion and in-cylinder process through deviations in the Seiliger process parameters derived from the above mentioned engine measurements [58]. The same

characterization methodology was applied to model the in-cylinder process for different blends of carbon dioxide and natural gas (CO_2-NG). Based on the derived Seiliger parameters, parametric equations were derived to simulate the in-cylinder process for varying anode-off gas and natural gas fuel blends that could not be experimentally tested. This in-cylinder model was combined with a mean value engine model (MVEM) to capture the complete engine performance for varying blends of anode-off gas and natural gas. The developed in-cylinder modelling approach and the MVEM were validated against engine measurements. Next, the developed AOG-NG MVEM in combination with the SOFC model was employed to investigate the potential of SOFC-ICE integration for different current densities, pre-reforming ratios, fuel utilizations and load sharing strategies. The variables used to evaluate system performance are efficiency and emissions (of UHC, CO_2 and NOx) along with space and weight considerations. After the SOFC-ICE integration analysis, the 0-D SOFC model was used to compare the load response of the SOFC against that of the ICE to discuss the dynamic capabilities from a maritime perspective. The load response of the ICE was based on engine experiments and has been covered in Section 6.2.

To capture the in-cylinder process, the average in-cylinder pressure and crank angle measurements obtained from the steady state engine experiments were used as a starting point for the Seiliger-based combustion characterization process and models used in the third step of the research methodology as shown in Fig. 3. In this Seiliger-based combustion characterization approach, a heat release rate (HRR) model based on in-cylinder pressure and crank angle was developed. The outputs of this heat release model were used to develop the Seiliger-based combustion characterization or in-cylinder model, which is capable of capturing the effects of combustion in the form of variations in Seiliger combustion parameters for varying fuel blends, loads and even air-excess ratios or engine leaning. The details of the HRR model, the Seiliger in-cylinder model along with the Seiliger parameters can be found in the previous research paper by the authors [58]. The developed Seiliger-based in-cylinder model is further integrated with a MVEM to simulate the entire engine performance as explained in the previous paragraph. In the HRR model, the average in-cylinder temperature is calculated based on measured variables of in-cylinder pressure and crank angle. Therefore, the in-cylinder temperature obtained from the HRR model is referred to as the measured in-cylinder temperature for all the subsequent sections in this paper [58].

In this paper, all the simulation and modelling results are presented at the NOx value of 500 mg N m^{-3} (for 5% reference oxygen). The 500 mg N m^{-3} of NOx value is lower than the NOx IMO Tier-III limit for this engine, which is 2.08 g kW^{-1} h. During experiments, the measurements with different hydrogen and carbon dioxide percentages were restricted to the maximum load setpoint of 75% load. This is because, at 90% load with only natural gas (ONG), the engine was operating close to its
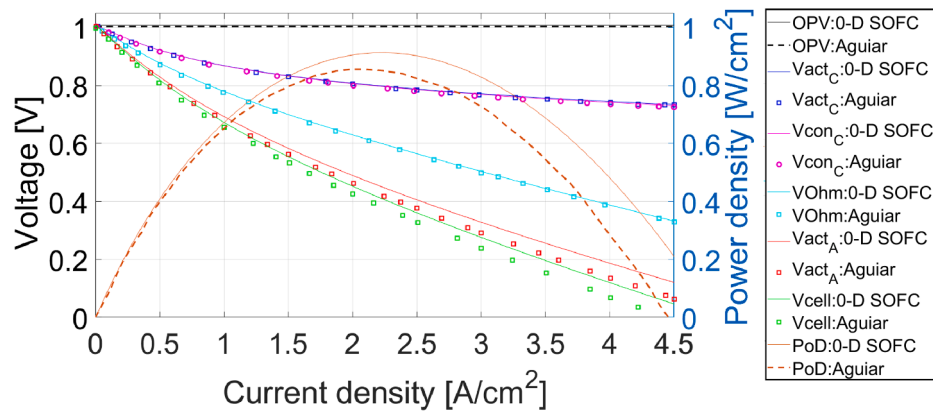
Fig. 4. i-V and PoD curve with cell losses at 1073 K for undepleted fully reformed mixture.

turbocharging limit, i.e., it was not possible to lean out the engine to 500 mg N m^{-3} of NOx at higher percentages of hydrogen.

3. SOFC model, verification and performance analysis

3.1. SOFC single cell model description and assumptions

In current literature, SOFC models vary from electrode and/or electrolyte level to system level models. SOFC performance modelling can vary by the degree of complexity, details and computational effort required. 0-D to 3-D models are available for modelling of SOFC stack performance [59,60]. For the purpose of the research presented in this paper, system level modelling capable of computing the polarization curves, fuel cell efficiency, anode-off gas composition and flow rates is sufficient [31]. In this paper, SOFC stack performance is extrapolated from a single cell model.

To avoid the risk of carbon deposition and large temperature gradients in the cells [61], practical systems operate with a methane pre-reformer. Therefore, the modelled SOFC operates with a methane pre-reformer, which partially pre-reforms a fixed percentage of methane to hydrogen and carbon monoxide. In the single cell model, the incoming fuel rate or fuel utilization (ratio of fuel consumed to fuel supplied), current density, air-excess ratio and methane pre-reforming ratio are used as inputs to compute the cell performance. Based on these inputs, the cell model consists of a pre-reformer model, electrochemical model, equilibrium model, mass and energy balance solver to compute cell voltage, anode-off gas composition, anode-off gas flow rates, cell power, efficiency and temperature curves.

The pre-reformer model uses a prescribed methane pre-reforming ratio (PRR) to control the percentage of methane being pre-reformed. During pre-reforming, the required amount of steam is dictated by the prescribed steam-to-carbon ratio. The operating temperature of the pre-reformer is equal to the initial operating temperature of the SOFC. The pre-reformer model is adopted from [62]. The modelled pre-reformer simulates indirect internal reforming, thus, the heat required to maintain the reactions in the pre-reformer is obtained from the SOFC. In real systems, indirect internal reforming of methane is performed by re-formers positioned in close thermal contact with the stack [63]. In this SOFC model, the total heat required for pre-reforming the methane flow entering the stack is discretized. Therefore, the pre-reformer model is solved with the single cell model to account for the heat required for indirect internal reforming of the methane flow corresponding to each cell.

The equations for the electrochemical and the equilibrium model are based on [57,64,62]. The equilibrium model solves for chemical equilibrium and the conservation of elements H, C and O with cell temperature, fuel utilization and S/C ratio as inputs to determine the molar fractions of the four species present in anode-off gas, namely, H_2O, H_2,

CO and CO_2. CH_4 is assumed to be completely reformed and converted to H_2 in the anode-flow channel. The mass balance solver computes the mass flows inside the anode-flow and cathode-flow channels. During SOFC operation, energy is exchanged in the form of heat, chemical energy and electrical energy. To determine the cell operating temperatures, energy balance is solved for the anode-flow channel, cathode-flow channel, positive electrode–electrolyte-negative electrode (PEN) structure and the interconnect. The energy balance equations are based on [57,33,62]. The SOFC single cell model is based on cell geometry and material data presented in [57]. The reference cell data is for a planar, co-flow, anode-supported fuel cell. Appendix B.1 lists the main assumptions and considerations under which the single cell model operates.

3.2. SOFC cell-to-stack performance

Based on above described single cell model, single cell performance is extrapolated to estimate the stack performance. The SOFC stack consists of a number of cells with uniform performance. Therefore, the SOFC (DC) stack power is estimated by multiplying the number of cells with the current density, the cell voltage and the active cell area. Next, DC to AC conversion losses are considered by applying a conversion efficiency for the purpose of integrating with the engine (AC). Additionally, 5% auxiliary losses are added as parasitic power losses for the Balance of Plant (BoP) system.

After calculating the total SOFC power ($P_{SOFC,AC}$), SOFC efficiency is estimated by applying the following Eq. (3.1).

$$\eta_{SOFC} = \frac{P_{SOFC,AC}}{\dot{N}_{CH4}^{in} \cdot LHV_{CH4}} \tag{3.1}$$

where, '$\dot{N}_{CH4}^{in}$' is the molar flow rate of incoming hydrogen while 'LHV_{CH4}' is the lower heating value of methane, which is equal to 802.6 × 10^3 kJ mol^{-1} [65].

3.3. SOFC model verification

For the purpose of verification, SOFC cell model outputs are compared against the cell performance data provided by Aguiar et al. [57]. The electrochemical cell model is used to compute cell voltages and power density (PoD) curves against current density (i) for an undepleted fully reformed fuel mixture. Fig. 4 shows the current density–voltage (i-V) curves predicted by the electrochemical model for cell operating temperature of 1073 K. Activation, concentration and ohmic cell voltage losses have also been plotted and compared against data provided by Aguiar et al. As seen from Fig. 4, the open-circuit voltage, cathode activation potential, cathode concentration potential loss and ohmic losses match well with the literature data. However, there are

Table 1
Effect of fuel utilization on anode-off gas compositions [Volume%].

Fuel Utilizations	70%	75%	80%	85%
H_2O [%]	61.71	64.88	67.89	70.95
H_2 [%]	18.29	15.12	12.11	9.05
CO [%]	5.69	4.83	3.91	2.96
CO_2 [%]	14.31	15.17	16.09	17.04
CO_2/H_2	0.783	1	1.33	1.88

small deviations between the reference and simulated anode activation loss, which is transferred to a marginal deviation in the computed cell voltage (V_{cell}).

Fig. 4 also depicts the comparison between the simulated and reference power density at 1073 K. The computed power density compares well with the reference model, however, deviations arise after PoD of 10000 A m^{-2}. This divergence in PoD after 10000 A m^{-2} is due to the deviations in the anode-activation loss, which also leads to a difference in the estimation of operating cell voltage. The difference in anode-activation loss could be attributed to the difference in equations used by the cell model and the 1-D model by Aguiar et al. The 1-D model developed by Aguiar uses the Butler–Volmer equation to calculate the activation loss [57]. However, the current cell model employs the hyperbolic sine approximation [62], which represents the combined anode and cathode activation losses. The combined hyperbolic sine approximation is a widely employed method to calculate the loss in activation potential. Norren and Hoffman made a comparison of various approximations and recommended the hyperbolic sine approximation due to its superior accuracy over the majority of operating current densities [66]. Furthermore, deviations in cell performance prediction could be attributed to the difference in modelling approach of 0-D versus the 1-D model by Aguiar et al. Although the 1-D modelling approach can be more accurate in simulating cell performance compared to a 0-D model, the higher-level models require much more computational effort [62,33]. Therefore, for the SOFC-ICE system integration research presented in this paper, a 0-D SOFC model capable of capturing the polarization curves, cell temperatures, anode-off gas compositions and flow rates with good accuracy is found to be acceptable. For future research and improved accuracy in cell performance prediction, calibration of the 0-D SOFC model with experiments in addition to higher-level SOFC models is recommended.

To avoid large deviations in the estimation of cell voltage, the current density values assumed in this study for SOFC performance analysis are kept below 10000 A m^{-2}. The deviations at high current densities are also evident at operating temperatures of 973 K and 1023 K, as seen in Fig. B1 of Appendix B.2. The cell voltage and power density increase with increased cell temperature due to lower potential losses and improved reaction kinetics. The electrochemical model verification affirms the voltage and power density prediction capabilities of the cell model, which are essential for computing fuel cell efficiency. Besides efficiency, the model also calculates anode-off gas compositions, flow rates and cell temperatures due to changes in control parameters such as current density, pre-reforming ratio and fuel utilization. The impact of these control parameters on SOFC-ICE integration will be discussed in Section 5.

Increasing fuel utilization (U_f) can increase cell efficiency, however, operation at high fuel utilizations is restricted because a much higher contribution of concentration polarization and a high risk of fuel starvation is observed. Researchers have shown that local oxidations of the cells due to fuel starvation can be found irrespective of the applied fuel and current density, which adversely affect the lifetime of the cell [67]. For this reason, fuel utilization is kept below 85% for all following investigations presented in this research. On the other hand, low fuel utilization can significantly reduce SOFC efficiency. As fuel utilization decreases, higher percentages of hydrogen and carbon monoxide are available in the anode-off gas relative to water vapour and carbon

dioxide. Table 1 shows the anode-off gas compositions and flow-rates for fuel utilizations varying from 70% to 85%.

As seen in Table 1, water vapour forms the largest constituent of anode-off gas. Volumetric percentage of CO is small compared to the percentages of H_2 and CO_2. Furthermore, the amount of CO further decreases at higher fuel utilizations. The percentage of hydrogen relative to the percentage of carbon dioxide is more at 70% U_f, with equal amounts at 75% U_f. At higher fuel utilizations, carbon dioxide increases in comparison to hydrogen reaching a carbon dioxide to hydrogen ratio of about 1.88. For SOFC-ICE integration, anode-off gas compositions presented in Table 1 are directed from the SOFC to combust in the marine natural gas engine.

4. AOG-NG combustion, MVEM and validation

In this integration approach, water vapour in the anode-off gas is condensed out because SI natural gas engines can experience ignition and combustion instability problems with water vapour intake [68,50]. Operating the SOFC at different fuel utilizations and loads and the removal of moisture can provide a tailored gas quality and quantity, which can be blended with natural gas and combusted in the engine to meet the required power demand onboard a ship. In the dry anode-off gas, hydrogen and carbon monoxide are combustible products while carbon dioxide is inert, which can adversely impact the engine performance and integration with the SOFC. To investigate the potential of SOFC-ICE integration in terms of efficiency, emissions and load sharing, effects of combusting anode-off gas and natural gas blends in the SI engine need to be captured.

For this purpose, first, the effects of combusting blends of individual constituents of anode-off gas and natural gas were studied by performing experimental and simulation-based investigations. Next, by combining the effects of each constituent, combustion and engine performance was analysed for different anode-off gas and natural gas blends. In this research, the effects of carbon monoxide on the combustion process and engine performance are not considered. Appendix C.1 details the reasoning for neglecting the effects of carbon monoxide in this phase of the research.

In the research methodology followed, experiments were combined with Seiliger-based in-cylinder modelling and mean value engine modelling to simulate engine performance at different loads and blend percentages of hydrogen, carbon dioxide and natural gas based on anode-off gas compositions. The developed simulation models are validated against measurements and further used to capture the in-cylinder process and engine performance for test cases that could not be studied experimentally. Appendix C.1 and C.2 cover the description of the Seiliger-based combustion characterization and parametrization process used to capture the variations in the combustion and in-cylinder process for different blends of anode-off gas and natural gas. The appendix also covers an experimental validation of this methodology. The details of the experimental methodology have been provided in Section 2.

After capturing the in-cylinder process, the Seiliger in-cylinder modelling approach is combined with a mean value engine modelling approach to capture the complete performance of the AOG-NG engine. The AOG-NG engine is capable of operating on only natural gas, natural gas blended with hydrogen, natural gas blended with carbon dioxide and natural gas blended with hydrogen and carbon dioxide or the AOG-NG fuel blends. The MVEM is required for simulating the impact of varying AOG-NG fuel blends (based on SOFC operation) on turbocharging, manifold pressure control, emissions and load sharing. Furthermore, to integrate the SOFC with the engine in the proposed system, heat from the engine exhaust (temperature computed by the MVEM) is required to manage the heat balance within the system. The discussion in Appendix C.3 covers the description of the developed mean value engine model along with its various submodels. This section presents the validation of the AOG-NG MVEM.

To validate the AOG-NG MVEM, engine performance is simulated for

Table 2
Tested H_2-CO_2-NG fuel blends for 500 mg N m^{-3} of NOx at 75% load.

Composition No.	H_2 [Vol.%]	CO_2 [Vol.%]	NG [Vol.%]
1	15	15	70
2	12.65	12.65	74.7
3	9.2	17.5	73.3

Table 3
Simulated engine efficiency and error percentages between the simulated and measured values of performance parameters for the three anode-off gas and natural gas fuel compositions provided in Table 2 at 500 mg N m^{-3} NOx and 75% load.

Composition	η_{ICE} [%]	λ [%]	p_{bt} [%]	MAP [%]	p_d [%]	T_d [%]	T_e [%]
1	34.47	1.54	3.16	2.82	7.07	−0.2289	−3.28
2	34.17	0.81	3.38	3.75	6.46	−1.78	−5.17
3	33.80	0.58	2.57	2.21	7.29	1.51	−2.07

the three compositions listed in Table 2. Based on the anode-off gas compositions provided in Table 1, combined effects of combusting hydrogen and carbon dioxide together with natural gas are simulated and compared with experiments. The tested compositions of hydrogen, carbon dioxide and natural gas are given in Table 2. Composition 1 and 2 replicate the anode-off gas composition available at fuel utilization of 75% while composition number 3 corresponds to a much higher fuel utilization with a CO_2 to H_2 ratio of 1.9. These blends were experimentally tested at 75% engine loading and 500 mg N m^{-3} of NOx. In this manner, the combined blend of hydrogen and carbon dioxide forms the anode-off gas, which replaces natural gas going into the engine.

For MVEM validation, engine performance parameters such as air-excess ratio, charge pressure before throttle (p_{bt}), manifold pressure (MAP), exhaust receiver pressure (p_d), exhaust receiver temperature (T_d) and turbine outlet temperature (T_e) are compared against measurements. Table 3 shows the error percentages between the measured and MVEM simulated performance parameters for different fuel blends. The MVEM is able to capture the engine performance with sufficient accuracy for the three AOG-NG fuel compositions at 75% engine load. The maximum deviation was found to be about 7% for exhaust receiver pressure. Other engine parameters were simulated with error

percentages equal to or lower than 5%.

Table 3 also shows the simulated engine efficiencies for the three fuel compositions. The simulated and measured engine efficiency for ONG performance at 75% load is 33.68%. Composition 1 with 15% hydrogen and 15% carbon dioxide blend showcases the highest efficiency. The efficiency decreases with an increasing percentage of carbon dioxide with no significant penalty due to high CO_2 percentages at high fuel utilizations of 85%. Therefore, the simulations show that the AOG-NG engine is able to sustain the performance with possible efficiency improvements for different AOG-NG compositions based on SOFC fuel utilizations. Based on the validation and the confidence in engine performance simulation, the AOG-NG MVEM is further employed to study SOFC-ICE integration in combination with the presented 0-D SOFC model.

5. SOFC-ICE integration results

In this study, the impact of SOFC control parameters such as current density, pre-reforming ratio and fuel utilization on the efficiency of the SOFC-ICE integrated power plant is analysed. For this study, the following control and input parameters are kept constant for the models, unless mentioned otherwise. The fuel and air inlet temperatures are kept constant at 1073 K with ambient operating pressure. The current density is maintained at 5000 A m^{-2}, fuel utilization at 80% and the S/C ratio at 2. The air-excess ratio is controlled by a PI controller to keep the inlet and outlet temperatures of the cell within 100 K. This is done to maintain a thermal gradient of 10 K cm^{-1} and, thus, avoid thermal stresses due to large temperature gradients. The pre-reforming ratio (PRR) is fixed at 0.3 and the pre-reforming reaction heat is obtained for the SOFC. In this manner, the fuel cell heat is reused for chemical conversion in the pre-reformer to improve efficiency for a given fuel utilization [36]. Additionally, heat supplied to the pre-reformer helps reduce the amount of air needed to cool the cells. The number of cells in the stack is equal to 11000.

Additionally, all simulations are performed for a SOFC-ICE combined power output of 750 kWe. The blend percentages of hydrogen and carbon dioxide directed into the engine are based on the ratio of hydrogen and carbon dioxide present in the incoming SOFC anode-off gas. Since the AOG-NG MVEM has been validated for a maximum blend percentage of 30% AOG and 70% NG, the maximum blend percentage of anode-off gas in all the proceeding analysis is kept at 30%.
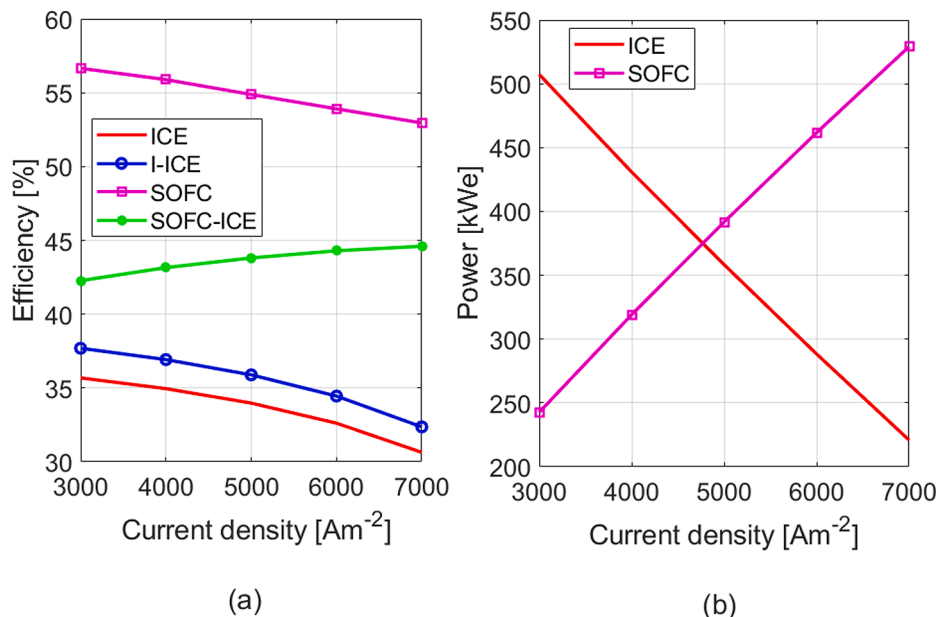

(a)   (b)

Fig. 5. Simulated efficiencies (a) and power outputs (b) for SOFC-ICE integration at different current densities with a total system power output of 750 kWe.
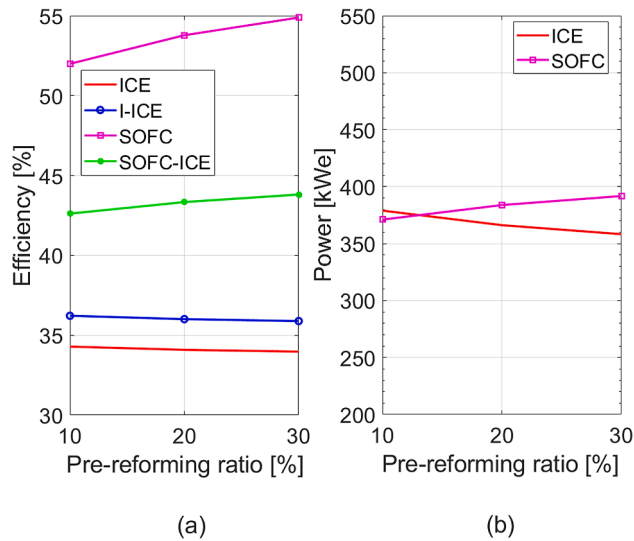
Table 4
Flow-rates of hydrogen and carbon dioxide present in SOFC anode-off gas for different fuel utilizations.

Fuel utilization%	$H_{2,SOFC}$ [m^3 h^{-1}]	$CO_{2,SOFC}$ [m^3 h^{-1}]
70	80.62	63.30
75	62.43	62.43
80	46.33	62.17
85	32.87	61.94

Table 5
Blend percentages and flow-rates of hydrogen and carbon dioxide (from SOFC anode-off gas) directed into the engine for different fuel utilizations.

Fuel utilization [%]	$H_{2,ENG}$ Vol. [%]	$CO_{2,ENG}$ Vol. [%]	$H_{2,ENG}$ [m^3 h^{-1}]	$CO_{2,ENG}$ [m^3 h^{-1}]
70	16.81	13.19	26.17	20.54
75	15	15	23.67	23.67
80	12.81	17.19	20.65	27.72
85	10.40	19.60	17.16	32.34

Fig. 6. Simulated efficiencies (a) and power outputs (b) for SOFC-ICE integration at different pre-reforming ratios with a total system power output of 750 kWe.

Fig. 5(a) shows the simulated efficiencies of the standalone AOG-NG engine, integrated AOG-NG engine, only SOFC and the SOFC-ICE system at different current densities. The difference between the standalone AOG-NG engine and the integrated AOG-NG engine lies in the method of efficiency calculation. The efficiency of the standalone AOG-NG engine (η_{ICE}) is computed from Eq. (C.2), which includes the energy contribution of hydrogen from the anode-off gas. On the other hand, the efficiency of the integrated AOG-NG engine (η_{I-ICE}) is calculated from Eq. (5.1), which excludes the incoming energy contribution of hydrogen since it is accounted for in the SOFC efficiency calculation. Therefore, the efficiency of the integrated AOG-NG engine is higher than the standalone AOG-NG engine efficiency. For the integrated SOFC-ICE system, the efficiency is calculated by applying Eq. (5.2).

$$\eta_{I-ICE} = \frac{P_{ICE}}{\dot{m}_{fuel}.LHV_{fuel} - \dot{m}_{H_2}.LHV_{H_2}} \quad (5.1)$$

$$\eta_{SOFC-ICE} = \frac{P_{SOFC-ICE}}{EC_{SOFC} + EC_{I-ICE}} \quad (5.2)$$

where '$P_{SOFC-ICE}$' is the total power output of the SOFC-ICE integrated system in kWe. 'EC_{SOFC}' represents the incoming energy contribution of the SOFC while 'EC_{I-ICE}' represents the incoming energy contribution of the integrated engine.

Increasing current density at constant fuel utilization adversely impacts the cell voltage but leads to an increase in the power produced by the SOFC. The increase in power comes at the cost of higher fuel intake, which results in reduced SOFC electrical efficiency with increasing current density as seen from Fig. 5(a). Furthermore, the increase in power produced by the SOFC leads to a reduced load on the engine since the combined SOFC-ICE power output is maintained at 750 kWe as seen from Fig. 5(b). Operation of the integrated AOG-NG engine at lower power outputs causes the engine efficiency to decrease at higher current densities. Although the efficiencies of the SOFC and the ICE decrease with increasing current density, the efficiency of the integrated SOFC-ICE power plant increases with increments in current density for a fixed total power output as seen from Fig. 5(a). The efficiency of the SOFC-ICE system increases because the power split favours the SOFC at higher current densities, which is more efficient than the engine. Although the efficiency of the integrated SOFC-ICE power plant improves at higher current densities for a fixed total power output, operation at high current densities can reduce fuel cell lifetime. Khan et al. found that during long-term testing voltage loss over time greatly

increases with higher current density leading to performance degradation [69]. Consequently, Aguiar et al. chose 5000 A m^{-2} as a suitable current density for their analysis as it provides a good balance between capital cost, efficiency, stable and realistic operation and power density [57]. Therefore, performance analysis in this research is performed at or close to 5000 A m^{-2}.

Contrary to current density, increments in methane pre-reforming ratio at constant fuel utilization and current density led to improvements in SOFC efficiency as depicted in Fig. 6(a). Increase in pre-reforming increases the operating cell voltage, which causes the SOFC power output to increase by a small amount as seen in Fig. 6(b). The increment in SOFC power is obtained while maintaining a constant fuel intake, thus, improving fuel cell efficiency. Since the fuel utilization is fixed at 80%, the ratio of hydrogen to carbon dioxide entering the engine is fixed at about 0.75. Increments in SOFC power output once again lead to lower loads share of the engine as seen in Fig. 6(b), however, the variations in power split with changing pre-reforming ratio are small. Therefore, the efficiency of the integrated AOG-NG engine marginally reduces with increase in pre-reforming. The small increase in SOFC load share and efficiency with increasing pre-reforming ratio leads to an increase in the overall system efficiency of the SOFC-ICE power plant as seen in Fig. 6(a). It is vital to note that increments in pre-reforming will increase the size of the pre-reformer, thus, reducing the power density of the system. Furthermore, increased pre-reforming will increase heat requirements from the SOFC and steam requirements, which could complicate and strain the Balance-of-Plant (BoP) and fuel cell operations. Therefore, in this research, a maximum pre-reforming ratio of 0.3 is maintained for all proceeding simulations.

To study the effects of varying fuel utilization, current density was kept constant at 4750 A m^{-2} while the remaining control and input parameters were fixed at default values provided at the beginning of this section. SOFC operation at different fuel utilizations is achieved by controlling the incoming methane fuel flow-rate. Fixing the current density at 4750 A m^{-2} helps in operating the SOFC close to 375 kWe, which helps in attaining a SOFC-ICE power split close to 50–50. The cell voltage simulated by the 0-D SOFC model reduces by a small margin with increasing fuel utilization while the current density and number of cells are kept constant. Therefore, the SOFC power simulated by the 0-D model varied from 376 kWe to 371 kWe for fuel utilizations varying from 70% to 85%. This small deviation from 375 kWe in SOFC power output keeps the power split between the SOFC and the engine close to 50–50 for different fuel utilizations.

Table 4 shows the flow rates of hydrogen and carbon dioxide present in the SOFC anode-off gas (after the removal of water vapour) for different fuel utilizations. For SOFC-ICE integration, the SOFC anode-off
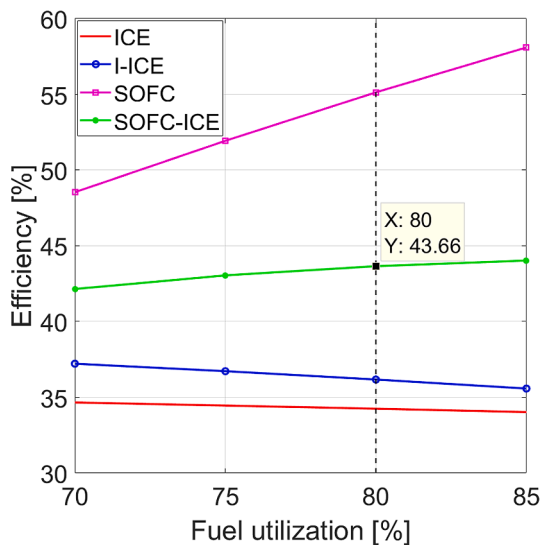
Fig. 7. Simulated efficiencies of SOFC-ICE integration for different fuel utilizations at a system power output of 750 kWe. Appendix D provides an example of efficiency calculation of the SOFC-ICE integration for the test condition depicted with a dashed vertical line in the above figure corresponding to 80% fuel utilization.

Table 6
Efficiency improvement for different fuel utilizations obtained from the SOFC-ICE integration compared to the standalone ONG marine engine performance at 750 kWe load.

Fuel utilization [%]	$\eta_{\text{Improvement}}$ [%]
70	5.35
75	6.24
80	6.85
85	7.22

gas is blended with natural gas and combusted in the AOG-NG engine. Therefore, the blend percentages of hydrogen and carbon dioxide directed into the engine are shown in Table 5. The blend percentages are based on the ratio of hydrogen and carbon dioxide present in the incoming SOFC anode-off gas. Fig. 7 shows the simulated efficiencies of the standalone AOG-NG engine, integrated AOG-NG engine, only SOFC and SOFC-ICE power plant for the different fuel utilizations.

The electrical efficiency (LHV) of the integrated system increases with increasing fuel utilization. As seen in Fig. 7, the efficiency of the integrated AOG-NG engine (blue line) is higher than the standalone AOG-NG engine (red line) efficiency by a maximum of 2.55% at 70% fuel utilization. This improvement increases to 3.55% when compared to a conventional marine engine operating on only natural gas and producing the same power output. The efficiency improvement is attained through a combination of improved combustion and replacement of natural gas fuel by hydrogen. As fuel utilization increases, the efficiency of the integrated AOG-NG engine decreases marginally due to the presence of significantly higher percentages of carbon dioxide than hydrogen in the AOG-NG fuel blend. The decrease in engine efficiency is more than compensated by the increase in SOFC efficiency at higher fuel utilizations as seen in Fig. 7. The integration between the SOFC and the integrated AOG-NG engine provides a maximum efficiency improvement of 7.2% at 85% fuel utilization in comparison to the simulated efficiency of the standalone marine engine operating on only natural gas at 750 kWe. Table 6 shows the efficiency improvement attained at different fuel utilizations from the SOFC-ICE integration compared to the standalone ONG marine engine efficiency at 750 kWe. The efficiency of ONG performance simulated by the MVEM for this conventional standalone marine engine at 750 kWe load is 36.80%.

The efficiency improvement obtained by integrating the SOFC and the AOG-NG engine for maritime applications is clearly visible from Table 6. SOFC operation at fuel utilizations from 70 to 85% can provide efficiency improvements of 5.3% to 7.2%. The SOFC operation is favourable at 80% fuel utilization as it ensures safe fuel cell operation, high SOFC efficiency and a good ratio of hydrogen and carbon dioxide in AOG-NG blend for improved engine operation. For this reason, the potential of SOFC-ICE is further investigated by fixing the SOFC fuel utilization at 80%.

For high-efficiency SOFC operation, the heat balance of the SOFC needs to be maintained ideally without external power supply. Therefore, heat management is vital for SOFC-ICE integration. Fig. 8 shows the heat balance of the integrated SOFC-ICE system for a 50–50 power split operation and 80% fuel utilization. Heat from the engine exhaust is utilized to partially superheat the steam while the heat required to further superheat the steam to input temperature of 1073 K is attained from the AOG_2 flow. The outcoming SOFC anode-off gas is split into two flows. AOG_1 flow is used to preheat the incoming methane flow in the pre-heater (P.H.1). At the same time, AOG_2 flow is utilized to superheat the steam to 1073 K, which is required for pre-reforming. After P.H.1 and superheating, the anode-off gas flows are combined before entering the cooler (C.O.). For SOFC-ICE integration, the moisture free AOG flow is attained by condensing out the water vapour from the AOG in the cooler. The dry anode-off gas is supplied to the marine SI AOG-NG engine for blending and combustion with natural gas. The incoming air is heated up to the inlet temperature by the outgoing depleted cathode air in the second pre-heater (P.H.2). Fig. 8 also shows the corresponding flow-rates needed for the heat balance. The presented heat balance proves that sufficient heat is available for successful integration of the SOFC and the engine. The balance-of-plant can be further optimised with numerous configurations. For instance, anode-off gas recirculation with or without a combustor can be adopted to directly supply the required heat and pre-reforming steam, thus, optimising the BoP [28]. By implementing a bypass for the anode-off gas, the percentage of anode-off gas recirculated and the amount supplied to the engine can be controlled for further optimization. The potential of anode-off gas recirculation for SOFC-ICE integration will be investigated in future.

In the next section, the potential of SOFC-ICE integration for maritime applications is discussed by exploring different power splits between the SOFC and the engine.

6. Discussion: Potential, SOFC-ICE load sharing and load response from maritime perspective

6.1. Potential and load sharing

The SOFC-ICE combined cycles (with a bottoming cycle approach) analysed in existing literature present a 13 to 15% load share of the engine [28,37,31], which corresponds to the engine output attained by directly combusting SOFC anode-off gas. Additionally, the power split favours the SOFC to attain high system efficiency. However, other operational requirements such as good transient capabilities, space and weight considerations and economics are critical for power generation onboard ships. A small load share of the engine could restrict the transient capabilities of the system as the load pick-up capabilities would be dictated by the SOFC, which could be limited for maritime applications. Section 6.2 analyses the dynamic capabilities of the SOFC and the ICE from a maritime perspective. Additionally, marine power generation with a large SOFC load share would require high capital expenditure in addition to high space and weight considerations. Therefore, power split favouring the SOFC load share may not be ideal for maritime applications.

Variations in power splits can help optimize SOFC-ICE integration for different ship types. Different ships have numerous operational profiles, which include various ship operations such as manoeuvring, range, cruising, acceleration, high speed, bollard-pull, etc. Therefore, power

Air in (SOFC): 0.7178 kg/s; Air out (SOFC): 0.6744 kg/s; CH_4 (SOFC): 0.013552 kg/s; Steam: 0.0304 kg/s; Economiser flow: 0.0304 kg/s; Evaporator flow: 2*Economiser flow; AOG: 0.0873 kg/s; Bypass AOG_1: 0.025152 kg/s; Bypass AOG_2: 0.062148 kg/s; Engine exhaust: 0.7850 kg/s; Cooling water: 0.8373 kg/s
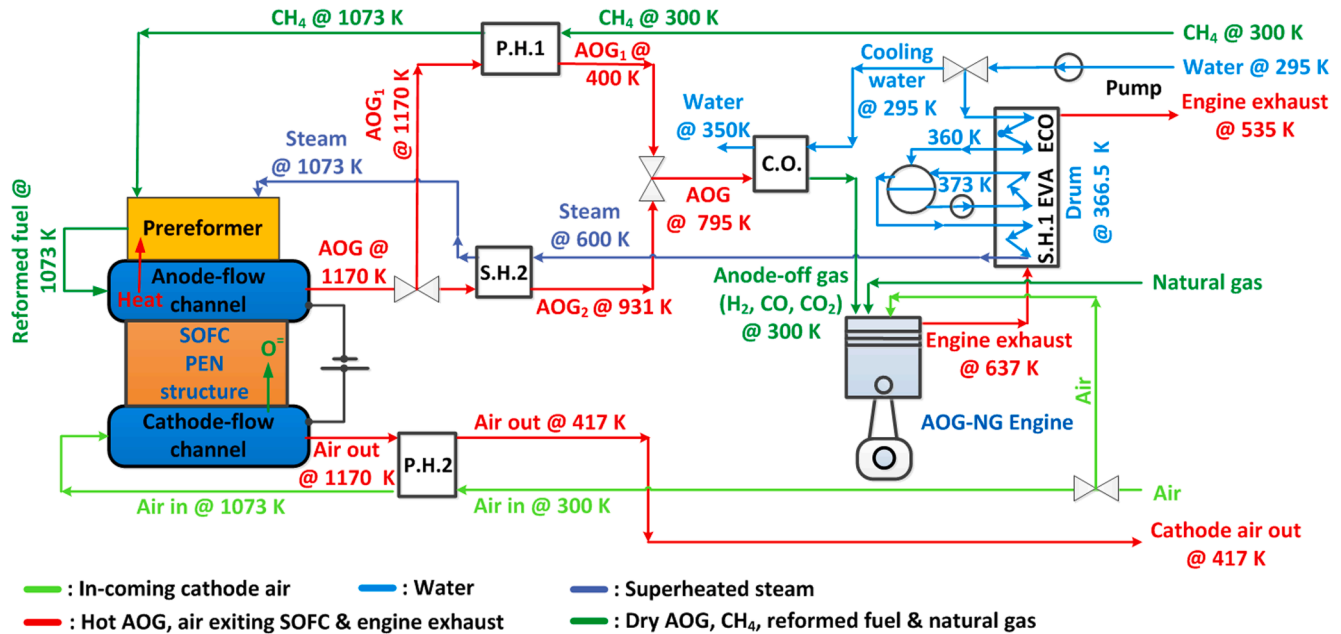

Fig. 8. Heat management for SOFC-ICE integration with 50–50 power split at 80% fuel utilization. P.H.: Preheater, C.O.: Cooler, S.H. Superheater, Evap: Evaporator, Eco: Economiser.

Table 7
Tested power splits (SOFC-ICE) with corresponding anode-off gas flow compositions and flow-rates.

Case	Cells	Power split [%]	Power split [kW]	$H_{2,SOFC}$ [m³ h⁻¹]	$CO_{2,SOFC}$ [m³ h⁻¹]
1	7000	33–67	250–500	31.03	41.67
2	10550	50–50	375–375	46.79	63.73
3	14000	67–33	500–250	62.06	83.26

Table 8
Anode-off gas flow compositions and flow-rates corresponding to the integrated engine for the three test cases with varying power splits.

Case	$H_{2,ICE}$ Vol. [%]	$CO_{2,ICE}$ Vol. [%]	$H_{2,ICE}$ [m³ h⁻¹]	$CO_{2,ICE}$ [m³ h⁻¹]
1	12.81	17.19	26.40	35.43
2	12.81	17.19	20.60	27.64
3	12.81	17.19	14.88	19.96

and transient operation requirements of ships can be significantly different [54,55]. For these reasons, the potential of SOFC-ICE integration proposed in this paper is investigated for different load sharing strategies in this section.

To investigate SOFC-ICE integration with different power splits, the rated power of the SOFC and engine is varied. The number of cells in the SOFC are varied for different power outputs while the current density and fuel utilization are fixed at 5000 A m⁻² and 80% respectively. Increasing the current density while keeping the number of cells constant for higher SOFC power outputs would adversely impact the SOFC efficiency. Furthermore, during long-term testing, Khan et al. found that voltage loss over time greatly increased with higher current density leading to performance degradation [69].

Table 7 shows the three different power splits investigated with total system power kept constant at 750 kWe. Furthermore, besides the number of cells, Table 7 also shows the flow rates of hydrogen and

carbon dioxide present in the SOFC anode-off gas after the removal of water vapour for the three load sharing strategies. After water vapour removal, anode-off gas is directed into the engine for blending with natural gas and remaining power generation. The AOG-NG blend ratios are fixed at 30–70 based on volumetric blend percentages. Table 8 shows the anode-off gas flow composition and flow rates of hydrogen and carbon dioxide utilised in the engine.

As seen in Tables 7 and 8, the percentage of hydrogen and carbon dioxide in AOG remains constant due to same fuel utilization, thus, fixing the blend ratio of carbon dioxide to hydrogen at 1.34. Fig. 9(a) shows the simulated efficiencies of the standalone AOG-NG engine, integrated AOG-NG engine, only SOFC and the SOFC-ICE system for different power splits. Additionally, Table 9 presents the efficiency improvements obtained for different power splits.

The efficiency of the SOFC remained constant for different power splits because the cell performance remains constant due to fixed fuel utilization and current density. The increased power output is achieved by increasing the number of cells as shown in Table 7. On the contrary, the efficiency of the integrated AOG-NG engine reduces with decreasing load share. The overall system efficiency increases with increasing load share of the SOFC. An efficiency improvement of 5.2% was found even for a 33–67 SOFC-ICE power split with a maximum improvement of more than 8% with a 67–33 load share.

It is evident from Fig. 9(a) and Table 9 that a significant efficiency improvement is attainable by integrating a small SOFC with a larger engine. The smaller load share of SOFC can help meet all the base or constant load requirements with continuous SOFC operation. At the same time, higher loads and load transients can be accommodated by the integrated AOG-NG engine leading to improved efficiency. Furthermore, there is a potential to further improve the efficiency for SOFC-ICE integration, since higher amounts of hydrogen are available for consumption inside the engine than the amount tested in this paper. The higher availability of hydrogen for blending and combustion in the engine is evident from Tables 7 and 8.

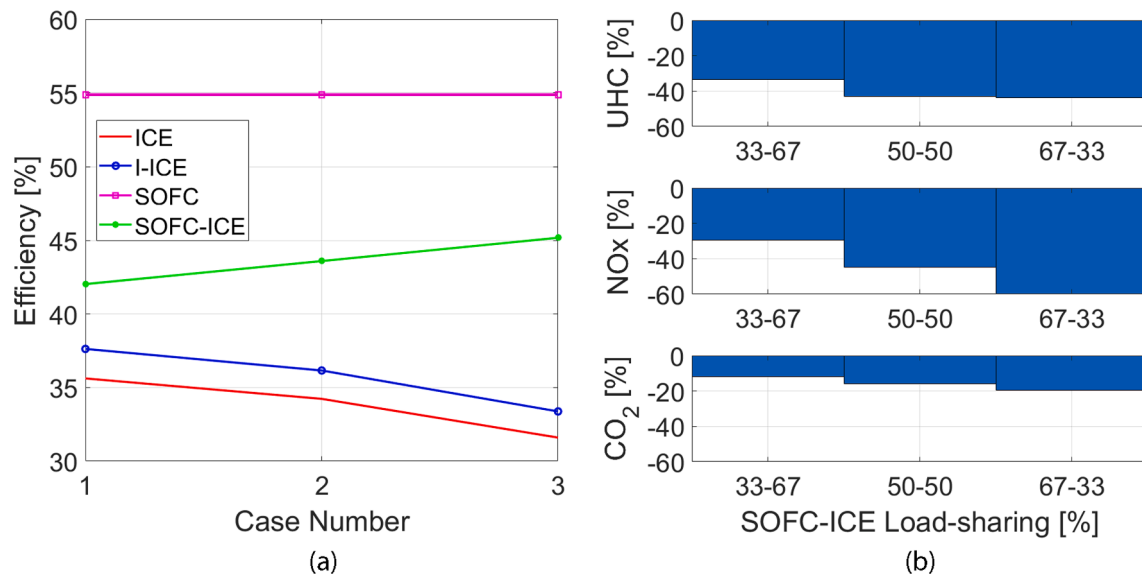To implement the SOFC-ICE combined cycle for maritime

Fig. 9. Simulated efficiencies (a) and emission reduction [%] (b) of SOFC-ICE integration for different power splits at a system power output of 750 kWe. All emissions are calculated in g kW^{-1} h^{-1}.

Table 9
Efficiency improvement for the three test cases of varying power splits obtained from the SOFC-ICE integration compared to the standalone ONG marine engine performance at 750 kWe power output.

Test case	$\eta_{\text{Improvement}}$ [%]
1	5.23
2	6.79
3	8.37

Table 10
Gravimetric and volumetric densities of a standalone engine and SOFC-ICE integration for the three power splits presented in Table 7 with the same rated power outputs of 750 kWe. [PS = SOFC-ICE Power split].

	Engine	PS: 33–67	PS: 50–50	PS: 67–33	PS: 85–15
Gravimetric density [W kg^{-1}]	69.93	39.28	32.22	27.31	23.39
Volumetric density [W L^{-1}]	33.72	18.96	15.55	13.19	11.30

applications, other factors such as environmental impact, system size and weight also need to be considered. Fig. 9(b) shows the improvement in harmful ship emissions, namely, unburnt hydrocarbons, CO_2 and NOx. The UHC and NOx emissions are engine-out emissions while CO_2 emissions from both the SOFC and the engine are taken into consideration. For a 50–50 power split, UHC and NOx reduction of about 40% is achievable in comparison to a conventional marine only natural gas engine of same power output, which are already capable of meeting IMO Tier-III regulations. Although there are no global emission regulations for methane, methane slip from natural gas-fuelled marine engines is identified as a serious concern for maritime applications due to its significant global warming potential [70]. Therefore, the reductions in UHC (methane) emissions found in this research for SOFC-ICE integration are of high significance for maritime applications as increasing number of natural gas-fuelled ships are being built and operated [71], which can employ the proposed system. Furthermore, carbon dioxide reductions range from 12 to about 20%. Significant emission reductions in UHC and NOx can be achieved from SOFC-ICE integration even when

the power split favours the engine.

Table 10 shows the gravimetric and volumetric densities of the systems for the three power splits in comparison to an engine with the same total power output. The computed gravimetric and volumetric density of the SOFC are 20.93 W kg^{-1} and 10.11 W L^{-1}, respectively. These values are based on the data found for a standalone SOFC of 300 kWe rated power [72]. The values were found to be the highest for a commercially available system [73,74]. For the engine, system size and weight densities are based on the data found for a commercially available NG SI engine of 400 kWe power output [75]. Table 10 provides the gravimetric and volumetric density of the ICE.

An increasing percentage of SOFC load share leads to significant increments in system size and weight. Although a 33–67 SOFC-ICE power split requires about 1.7 times the space and weight considerations, a 67–33 split is about 2.5 times larger and heavier in comparison to the engine. Additionally, Table 10 also shows that an 85-15% SOFC-ICE power split, which matches with the SOFC-ICE combined cycles analysed in existing literature would be about 3 times larger and heavier than the engine. Therefore, by employing the SOFC-ICE integration proposed in this paper for maritime applications, promising improvements in efficiency and emission reductions can be achieved with comparatively smaller increments in size and weight for a 33–67 power split. Furthermore, the efficiency improvements and emissions reductions are attained with a commercially existing engine.

In addition to the potential shown in this paper, SOFC-ICE integration has additional unexplored potential that can initiate a paradigm shift in ship performance and operations. For instance, if a flexible fuel blend AOG-NG engine capable of operating on any blend of anode-off gas and natural gas can be developed, unprecedented efficiency improvements could be gained at part and full load operation of the system. At part loads, beyond SOFC load share, efficiency could be enhanced by generating additional engine power on only SOFC anode-off gas. At even higher part loads, the amount of natural gas blended with anode-off gas could be increased for more engine power to generate the required increments in system load. At these higher load percentages, the engine (and the system) could operate at high efficiencies on blends with larger percentages of anode-off gas than natural gas. Therefore, further research should be performed to investigate the operation of marine engine at different loads on only anode-off gas and AOG-NG blends with percentage of anode-off gas greater than 30%. Besides natural gas, methanol and ammonia powered SOFC-ICE marine power plants should
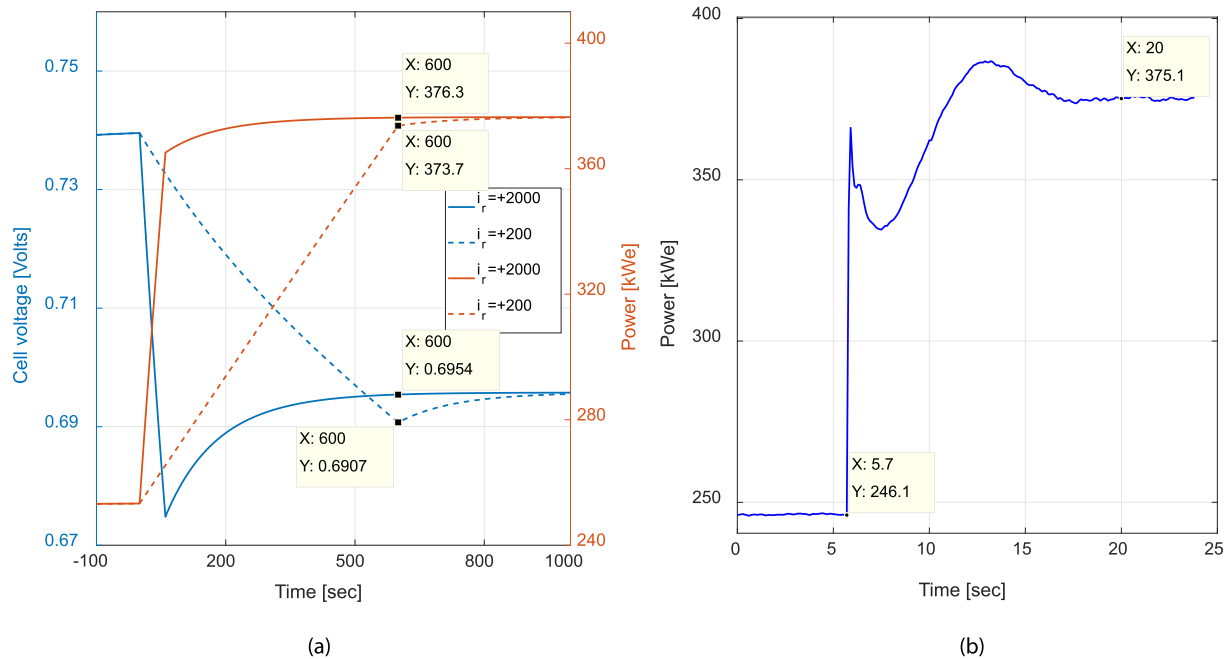
Fig. 10. Comparison between the dynamic response of SOFC (a) and ICE (b) for load change from 250 to 375kWe. In (a) response of fuel cell voltage and AC power output have been plotted. 'i$_r$' is the current density ramp rate measured in A m^{-2} min^{-1}.

be researched in future because of the increasing interest of the maritime industry in these fuels due to their potential of renewable production and substantially low emissions.

6.2. Load response of SOFC vs ICE: maritime perspective

The dynamic load response of the integrated SOFC-ICE system can impact system design, control and optimization. An investigation into the dynamic capabilities of the individual power components is crucial for the development of the integrated system from a maritime perspective. Therefore, in this subsection, the dynamic capabilities of the SOFC and ICE are compared for the same load pick-up.

To investigate the dynamic response of the SOFC, the capabilities of the 0-D SOFC model were first verified by comparing against the dynamic results provided by Salogni et al. for same test conditions [33,76]. Salogni et al. simulated the dynamic response with a 1-D model verified with the same fuel cell data available from Aguiar et al. for a planar IT-SOFC [57]. Appendix E covers the verification of the dynamic simulation capabilities of the 0-D SOFC model.

Based on this verification, the 0-D SOFC model was used to simulate the change in load demand from 250 kWe to 375 kWe. The total number of cells was fixed at 11000. For this simulation study, all model input parameters remained the same as the ones setup for the verification in Appendix E except for current density. The initial current density was changed to 3450 A m^{-2} corresponding to the power output of 250 kWe. In this subsection, the SOFC dynamic load response is discussed by focussing on stabilization time and ramp rate limitations. Therefore, to simulate the load change to 375 kWe, first, an optimistic current density ramp of +2000 A m^{-2} min^{-1} was simulated to discuss the stabilization time parameter. Second, the same load change was performed with a current density ramp rate of +200 A m^{-2} min^{-1} (10 times slower). In practical SOFC systems, ramp rates prescribed by the manufacturer are limited to values such as +200 A m^{-2} min^{-1} to allow the BoP components to respond accordingly and maintain, among others, fuel supply, air supply, the peak temperatures and temperature gradient within the operational limits of the stack [77]. Fast ramp-up rates can lead to high thermal gradients, which can damage the stack. One of the expected consequences of large thermal gradients can be cracking of the

glass–ceramic sealing that joins the fuel cell to the interconnect and makes the anode and cathode volume channels gas tight [78].

Fig. 10(a) shows the dynamic load response of the SOFC in terms of the power output and cell voltage. The cell voltage response corresponding to the +2000 A m^{-2} min^{-1} ramp rate is similar to the response discussed in Appendix E. In response to this current ramp, the electrochemistry and, thus, the voltage respond instantly increasing the power output to 365 kWe in about 60 s, however, the SOFC takes almost 500 to 600 s to reach steady state and the required load demand of 375 kWe due to the thermodynamic response lag [33,52]. The thermodynamic response lag has been discussed in Appendix E while the high stabilization time corresponding to the optimistic ramp rate of +2000 A m^{-2} min^{-1} can be seen in Fig. 10(a). This long stabilization time can pose a challenge in a dynamic loading environment like maritime since long stabilization times can make the SOFC vulnerable to thermal overloading and stressing of cells in case of frequent load changes [55].

Contrary to the ramp rate of +2000 A m^{-2} min^{-1}, the SOFC has a much smaller voltage undershoot and a much shorter stabilization time for the +200 A m^{-2} min^{-1} ramp rate, as seen in Fig. 10(a). However, for the practical +200 A m^{-2} min^{-1} ramp rate, the SOFC takes about 600 s to reach a value close to the required load of 375 kWe before the settling period starts, thus, showcasing the slow transient response of the SOFC. In addition to this, Biert et al. found that a PID air flowrate controller was unable to keep the maximum PEN temperature gradient below the advised value of 10 °C cm^{-1} for the manufacturer prescribed ramp rate of +200 A m^{-2} min^{-1} [60]. Furthermore, Andrea et al. found that a maximum current ramp rate of only +0.3 A min^{-1} (+30 A m^{-2} min^{-1}) was feasible without encroaching beyond the operating temperature limit given by the manufacturer [78]. This lower maximum ramp rate of +0.3 A min^{-1} would correspond to an even larger timescale than 600 s to achieve the required load change. Therefore, it is clear from the above discussion that the ramp rate and the dynamic capabilities of the SOFC are currently limited.

In comparison to the several hundreds of seconds taken by the SOFC, the ICE operating on only natural gas took about 14 s for the same load change from 250 kWe to 375 kWe, based on experiments. Fig. 10 shows the comparison between the time scales of the SOFC and the ICE for the same load change. The dynamic load response of the ICE was measured

on the lean-burn, spark-ignited, natural gas test engine used in this research. The load response was measured at 1500 rpm and fixed initial NOx of 500 mg N m^{-3}. The spark-timing for these engine experiments was fixed at 24° CA BTDC.

Based on the comparison presented in Fig. 10, it is evident that large and fast load changes could be challenging to meet with a SOFC. Depending on the application, operating conditions and ship operations, load demand in maritime can be close to fixed for hotelling and propulsion, however, changes in load demand can also be sudden requiring large load changes in tens of seconds. For instance, Taskar et al. showed that for a ship in head waves during harsh weather conditions, power fluctuations of 40% of rated power can be encountered in about 10 s [55,79]. Similarly, Theotokatos simulated the transient behaviour of a merchant ship (bulk carrier) under both acceleration and deceleration operating conditions [54]. The author showed that the effective power of the power generation unit (diesel engine) during acceleration increased from about 3000 kW (26% of rated power) to 7000 kW (about 61% of rated power) in about 120 s. Comparatively, the SOFC took about 600 s to change the load from 250 kWe to 375 kWe, as seen from Fig. 10(a). At the same time, the NG-fuelled test ICE took about 14 s for the same load change of 25% rated power (500 kWe), as explained earlier. Therefore, it is clear from the above discussion that the NG-fuelled ICE has better dynamic load response capabilities than that of a SOFC for maritime applications.

Thus, in the SOFC-ICE system proposed for maritime applications, a power split that favours the ICE would significantly improve the dynamic capabilities of the combined system and the possible sudden and large load changes can be met by the ICE.

7. Conclusions and recommendations

In this paper, a novel solid oxide fuel cell and internal combustion engine (SOFC-ICE) integration approach was proposed and investigated for maritime applications. SOFC-ICE integration was achieved by blending the SOFC anode-off gas with natural gas (AOG-NG) and combusting in a lean-burn, spark-ignited (SI) marine engine for additional power generation. A combination of zero-dimensional (0-D) SOFC cell-to-stack performance modelling, engine experiments, in-cylinder combustion modelling and mean value engine modelling was used to study the potential of SOFC-ICE integration for different current densities, pre-reforming ratios, fuel utilizations and load sharing strategies. The potential evaluation of the system was based on efficiency, space and weight considerations and emissions of unburnt hydrocarbons (UHC), nitrogen oxides (NOx) and carbon dioxide (CO_2). Numerous conclusions can be drawn from the research presented in this paper, which are as follows:

- Increments in both current density and pre-reforming ratio showed increments in SOFC-ICE power plant efficiency due to an increase in the SOFC load share.
- The efficiency of the integrated AOG-NG engine was enhanced by a maximum of 3.55% at 70% fuel utilization. SOFC-ICE integration, with a 50–50 power split at a 750 kWe power output and 85% fuel utilization, yielded a maximum efficiency improvement of 7.2% over a conventional marine natural gas engine with same power output. At high fuel utilizations, the marginal decrease in engine efficiency improvement due to high carbon dioxide percentages in AOG-NG fuel blends was more than compensated by the increase in SOFC efficiency.
- The SOFC-ICE power split of 67–33 showed the highest efficiency improvement of about 8%, while UHC and NOx emissions reduced by about 43% and 60% in comparison to a conventional marine natural gas engine. Furthermore, carbon dioxide (CO_2) emissions reduced by 20.74%. However, the 67–33 power split also accounted for space and weight increments of approximately two and a half times.

- For maritime applications, promising improvements in efficiency of 5.2%, UHC and NOx reductions of about 30% and CO_2 reductions of about 12% can be achieved from a 33–67 SOFC-ICE power split with comparatively much smaller increments in size and weight of 1.7 times compared to a conventional marine natural gas engine. This research shows that significant enhancements in efficiency and reductions in emissions can be attained by integrating the SOFC with a commercially existing engine technology.
- Furthermore, the 0-D SOFC model simulations showed that the SOFC took about 500 to 600 s to reach steady state (for a +2000 A m^{-2} min^{-1} ramp rate) and 600 s to reach the required load (for a +200 A m^{-2} min^{-1} ramp rate) during a load change from 250 to 375 kWe. Comparatively, the ICE achieved the same load change in about 14 s based on dynamic engine experiments. The study concluded that in the SOFC-ICE system proposed for maritime applications, a power split that favours the ICE would significantly improve the dynamic capabilities of the combined system and the possible sudden and large load changes can be met by the ICE.

The following recommendations are proposed for future work:

- The 0-D SOFC model should be further calibrated and validated against experimental data. Heat transfer from the SOFC stack should be taken into consideration.
- The effects of carbon monoxide (CO) should be considered in future when testing higher blend percentages of AOG to account for the possible positive impact of CO on SOFC-ICE integration.
- Further research is recommended to investigate the operation of marine engine at different loads on only anode-off gas and AOG-NG blends with percentage of anode-off gas greater than 30%. Besides natural gas, methanol and ammonia powered SOFC-ICE marine power plants are recommended for future research.
- A 1-D SOFC model is recommended to more accurately capture the temperature variations and voltage response during transients while accounting for maximum thermal gradients and stresses.

CRediT authorship contribution statement

Harsh Sapra: Conceptualization, Methodology, Software, Formal analysis, Investigation, Data curation, Writing - original draft, Visualization. **Jelle Stam:** Conceptualization, Methodology, Investigation, Writing - review & editing. **Jeroen Reurings:** Methodology, Software, Investigation, Writing - review & editing. **Lindert van Biert:** Conceptualization, Writing - review & editing. **Wim van Sluijs:** Resources, Data curation, Investigation. **Peter de Vos:** Conceptualization, Writing - review & editing, Supervision. **Klaas Visser:** Conceptualization, Writing - review & editing, Supervision. **Aravind Purushothaman Vellayani:** Conceptualization, Writing - review & editing. **Hans Hopman:** Conceptualization, Supervision.

Declaration of Competing Interest

The authors declare that they have no known competing financial interests or personal relationships that could have appeared to influence the work reported in this paper.

Acknowledgements

Appendix A. Engine test setup

Experiments were performed on a 500 kWe, lean-burn and turbocharged marine SI natural gas engine with zero valve overlap. The test engine was connected to a generator to apply the load at 1500 rpm. Engine measurements were performed at varying engine loads of 75%, 50% and 25% at rated rpm. To study the effects of hydrogen and carbon dioxide addition based on SOFC anode-off gas, natural gas was replaced by different percentages of hydrogen and carbon dioxide, by volume. The tested engine blends have been presented in Section C.1. Additionally, experiments were also performed at different values of air-excess ratio to control the NOx emissions for each combination of fuel blend and engine load. For this purpose, engine performance was first measured at a fixed load point and NOx value, and then the engine was leaned, by increasing the air-intake (air-excess ratio) via manual control, to a lower value of NOx measured in mg N m^{-3} (at 5% reference oxygen). In this manner, engine performance for a fixed fuel blend and load was measured at different NOx values till misfire as shown in Table C1. For only natural gas (ONG) fuel and 500 mg N m^{-3} of NOx at 75% load, the value of air-excess ratio was higher than 1.6 and increased with engine leaning, thus, representing the lean-burn operation [80].

Natural gas flow was injected in the engine before the turbocharger and the flow was measured using a flowmeter. Hydrogen and carbon dioxide stored in pressurized bottles were injected in the natural gas line before the turbocharger, and the flow of blended gases was controlled via a mass flow meter. During these experiments, temperatures, pressures and flow rates were measured at different locations within the test setup, which have been depicted in Fig. A1. A schematic representation of the test setup including the hydrogen addition setup has been presented in Fig. A1. Cylinders 1, 2, 3 and 4 were equipped with a water-cooled Kistler 7061B sensors for in-cylinder pressure measurements. The sensors were flushed in each cylinder head to record a clean pressure signal. The in-cylinder pressure data was continuously measured in sets of 147 consecutive cycles at each measurement point using the Kistler Ki-Box measurement unit [81].
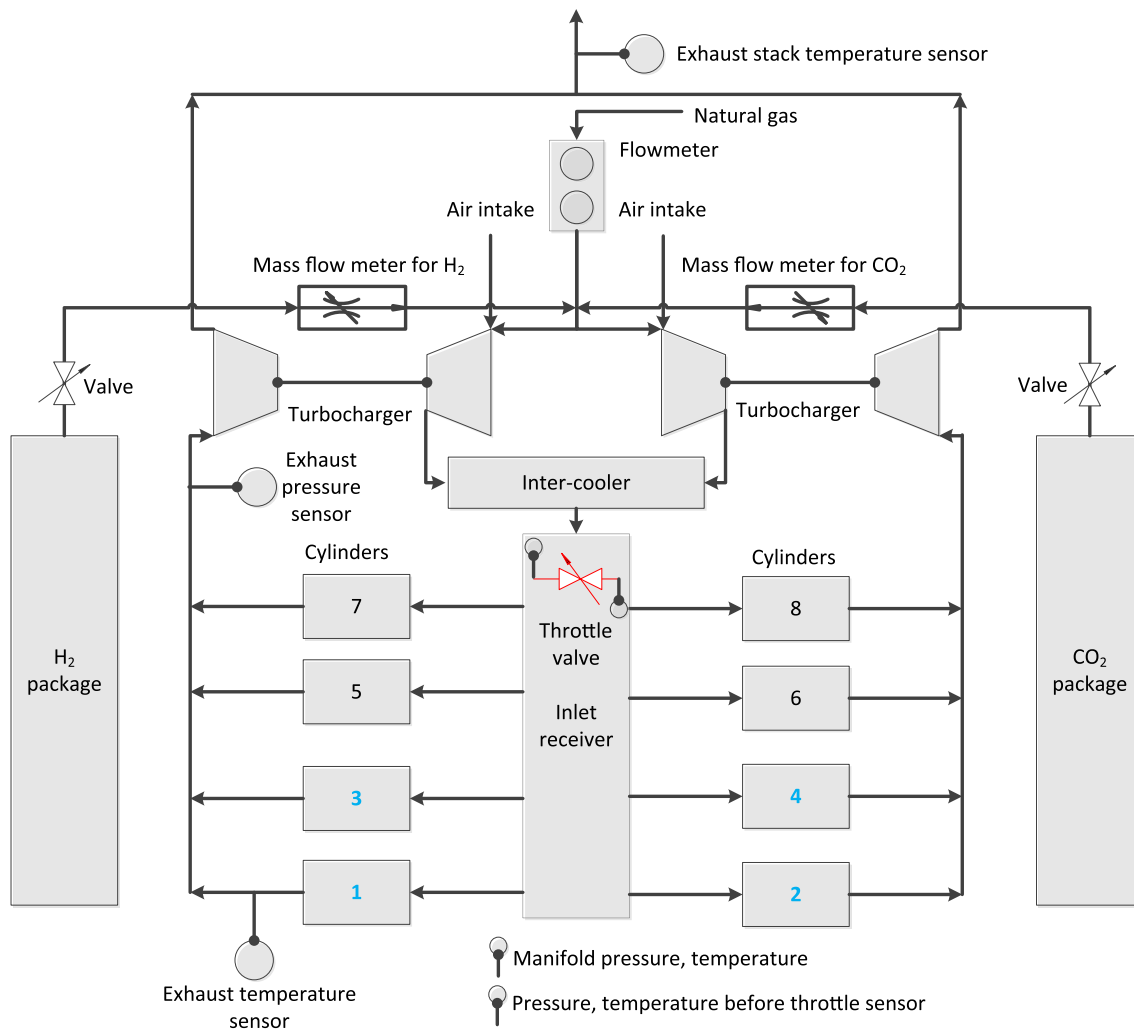

Fig. A1. Schematic representation of the engine test setup.

Appendix B. SOFC model assumptions and additional verification

B.1. SOFC model assumptions

- The SOFC model operates on 100% methane [57,82]. In reality, natural gas can contain small percentages of sulphur, which can poison the anode and reduce the catalytic activity [83,84]. Therefore, SOFCs operating on natural gas require a sulphur removal system. However, for system level modelling and dynamic modelling, this effect can be neglected [28,60].
- All gases in the SOFC follow the ideal gas law due to operation at high temperatures (higher than 1000 K) and ambient pressure.
- Pressure differences along the anode-flow and cathode-flow channels are assumed to be insignificant.
- The electrochemical oxidation of CO is neglected. Electrochemical reaction of CO is 2–5 times slower than that of hydrogen, therefore, carbon monoxide is considered to be consumed via the water–gas-shift reaction (WGS) [85].
- Pre-reformer is integrated with the SOFC to allow for indirect internal reforming. The heat for maintaining the reforming reactions is taken from the SOFC, therefore, the pre-reformer operates at the same temperature as the SOFC.
- Methane is completely reformed via indirect internal reforming (pre-reformer) and direct internal reforming.
- The MSR and WGS reactions are assumed to be fast enough to achieve chemical equilibrium [31].
- Adiabatic boundary conditions are assumed for the stack, i.e., heat loss to the surroundings is neglected.
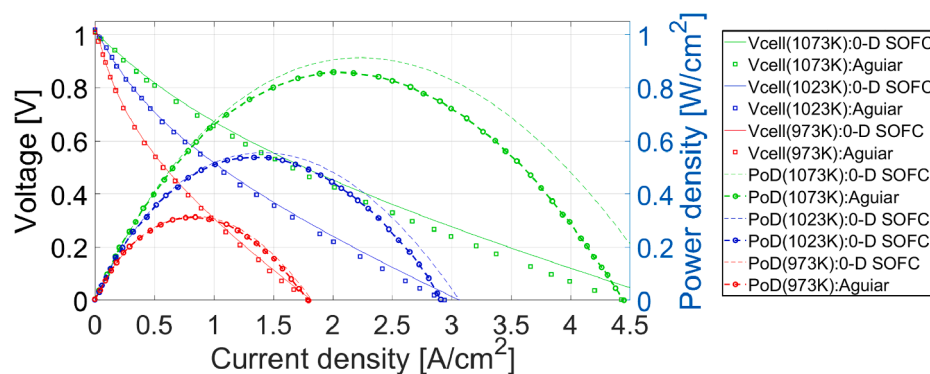
B.2. Additional model verification

See Fig. B1.

Fig. B1. i-V and PoD curves at 973, 1023 and 1073 973 K for an undepleted fully reformed mixture.

Appendix C. AOG-NG combustion characterization, validation and MVEM description

C.1. Combustion characterization and parameterization

In the previous research paper [58], the authors presented a methodology to characterize the H_2-NG combustion process based on engine measurements by using the Seiliger modelling approach, which discretizes the in-cylinder process in five discrete thermodynamic stages. Three stages describe the combustion process in the form of isochoric, isobaric and isothermal processes, which combined with the polytropic compression and expansion process capture the in-cylinder process. The effects of engine leaning and hydrogen addition at different engine loads were investigated using Seiliger in the previous study. The research found that Seiliger parameters 'a' (for the isochoric part), 'b' for (the isobaric part) and 'c' (for the isothermal part) represent different physical phenomenon in the H_2-NG combustion process. Furthermore, the authors concluded that at a fixed engine load and NOx value, all the effects of hydrogen addition on engine performance could be understood as deviations from the benchmark performance of the engine operating on only natural gas. Therefore, the H_2-NG and CO_2-NG combustion process can be studied in terms of deviations in Seiliger combustion parameters for different hydrogen blend percentages, carbon dioxide blend percentages and engine loads at a fixed NOx of 500 mg N m^{-3} (5% reference O_2).

To understand the deviations in combustion parameters, first, the combustion parameters are computed for all H_2-NG fuel blends (5H_2-NG, 10H_2-NG and 20H_2-NG) and engine loads (25, 50 and 75%) by applying the combustion characterization approach for Seiliger described in [58]. Similarly, the Seiliger combustion parameters are calculated for all CO_2-NG fuel blends. Table C1 shows the test blends and loads used for characterizing CO_2-NG combustion. Next, the differences between the combustion parameters are computed for each H_2-NG CO_2-NG blend at every load. This difference or delta in combustion parameters from the benchmark values of only natural gas performance at a fixed load is used to account for the changes in the in-cylinder combustion process due to hydrogen addition at that engine load.

Table C1
Experimentally tested CO_2-NG blends for varying NOx values.

Engine Load [%]	CO_2-NG Blends	NOx [mg N m^{-3}]
75	5, 10, 15CO_2-NG	500
50	5, 10, 20CO_2-NG	500
25	5, 10, 20CO_2-NG	500

All the effects of hydrogen and carbon dioxide addition on engine performance could be understood as deviations from the benchmark perfor-mance of the engine operating on only natural gas. Following this idea, parametric equations are derived via multivariable regression, which relates this delta or deviation in each combustion parameter due to hydrogen addition and carbon dioxide addition as a function of the normalized natural gas fuel mass and the volumetric percentage of hydrogen and carbon dioxide in the blend. A parametric equation is also derived, which computes the Seiliger parameters for ONG combustion as a function of normalized natural gas fuel mass (load).

Using these parametric equations, Seiliger parameters for ONG combustion and the deltas in Seiliger parameters are calculated for the H_2-NG and CO_2-NG blend percentage. Then, the estimated values of these deltas in combustion parameters are added over the benchmark values of parameters of ONG combustion to predict the final value of combustion parameters for H_2-NG and CO_2-NG combustion. In addition to the Seiliger parameters, natural gas fuel mass, unburnt hydrocarbons (measured in ppmv) and an initial estimate of air-excess ratio due to hydrogen and carbon dioxide addition is also derived by using the same general form of multivariable regression. These performance variables are used in the MVEM to simulate the complete engine performance as will be explained in Appendix C.3. In the engine simulations, the Seiliger parameters, natural gas fuel mass and UHC (in ppmv) obtained from the parametric equations are used as final values to estimate the engine performance in the MVEM while the air-excess ratio obtained from the parametric equations is used as an initial value for the MVEM pre-simulation as will be explained is Appendix C.3.

Following the above-described methodology of parametrization, Seiliger parameters, natural gas fuel mass and UHC can be derived for different percentages of hydrogen and carbon dioxide from the anode-off gas. The combustion and in-cylinder process for a specific blend and engine load is simulated by using the derived combustion parameters in the Seiliger process model described in [58]. The Seiliger process model is an in-cylinder model that simulates the combustion and in-cylinder process as a 5-stage discretized Seiliger cycle. Table C2 provides the error between the simulated and measured performance variables for 20H_2-NG fuel blend at 75% load and 20CO_2-NG fuel blend at 50% load.

As seen from Table C2, the Seiliger-based modelling combined with the multivariable regression equations is able to accurately estimate the performance parameters, which is crucial in order to capture the effects of hydrogen addition from anode-off gas since hydrogen has a direct effect on the peak pressures and temperatures. It is also important to accurately compute the work done (in kJ) and net combustion heat (Q_{net} in kJ) as these parameters are direct indicators of engine performance. Estimation of these performance variables along with exhaust pressure and temperature at the end of expansion stroke is essential as they dictate the turbocharger performance and also turbine outlet temperature, which can be critical for system integration with SOFC as shown in Section 5. In this manner, the individual effects of hydrogen and carbon dioxide percentages from SOFC anode-off gas on engine performance are studied in this paper. These individual effects of both the anode-off gas constituents are combined to capture the in-cylinder process of the engine operating on different blends of hydrogen and carbon dioxide from anode-off gas.

The effects of carbon monoxide from the anode-off gas were not taken into consideration as the effects of CO were not considered to be significant in this phase of research because of the following reasoning. The percentage of CO in anode-off gas is small compared to the percentages of hydrogen and carbon dioxide. This CO percentage reduces even further in the AOG-NG fuel blends studied in this research. Although the volumetric lower heating value of CO is slightly higher than that of hydrogen [86], the energy input of the ICE due to CO addition for the 30–70 AOG-NG blends tested in
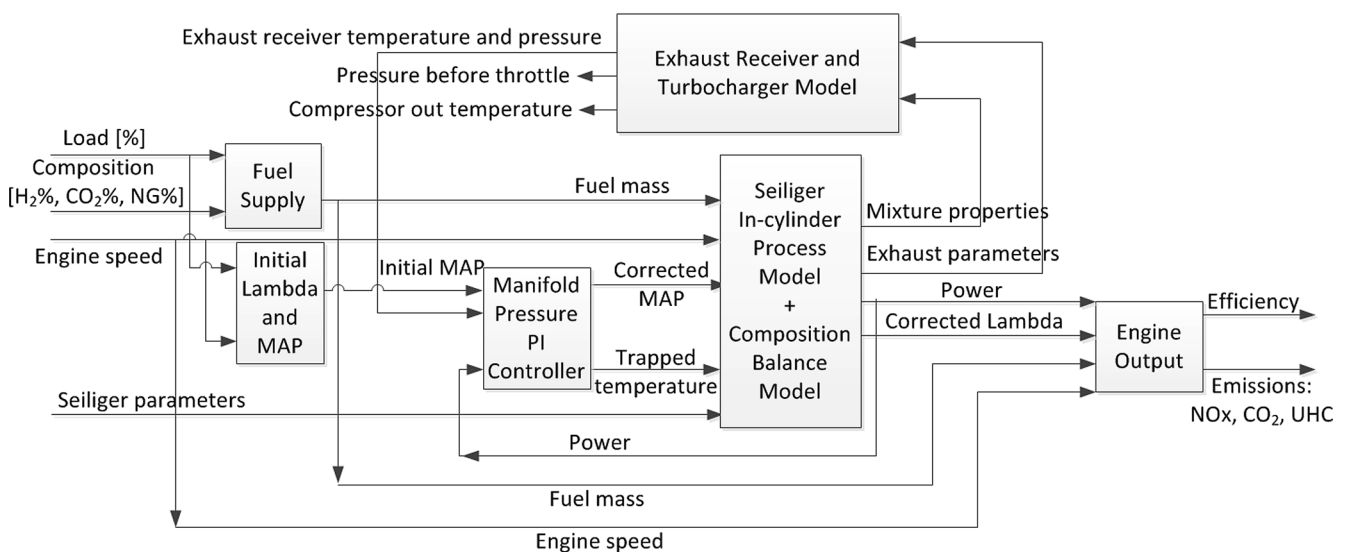
Fig. C1. Schematic representation of AOG-NG mean value engine model.

this research increases by only 1.2% compared to when CO is not considered. Therefore, the relatively smaller percentages of CO could support the combustion process and contribute to the engine efficiency like hydrogen, however, for the AOG-NG blends tested in this research, the impact would be non-significant. The effects of CO should be considered in future when testing higher blend percentages of AOG to account for the possible positive impact on SOFC-ICE integration.

C.2. Anode-off gas and natural gas blend combustion

Following the approach described in Appendix C.1, the effects of combusting a blend of hydrogen, carbon dioxide and natural gas can be simulated as a combined effect of deviations due to hydrogen and carbon dioxide relative to only natural gas combustion. Therefore, to simulate the in-cylinder process of the engine operating on anode-off gas-natural gas blends, the combined delta or deviation in Seiliger and performance parameters due to hydrogen and carbon dioxide percentages in the AOG-NG fuel blends are estimated by using the parametric equations explained in the preceding appendix. These derived parametric equations are for individual hydrogen and carbon dioxide percentages relative to 100% natural gas. Therefore, for a combined blend of hydrogen, carbon dioxide and natural gas, the percentage of hydrogen and carbon dioxide are recalculated relative to 100% natural gas and substituted in the derived parameters to estimate the delta in parameters.

The final values of the parameters for the AOG-NG blends are computed by adding the computed delta over the benchmark value computed for ONG. Table C3 shows the values of the estimated Seiliger parameters and natural gas fuel mass for the three compositions provided in Table 2 relative to only natural gas performance at 75% engine load. Table C3 also shows the measured natural gas fuel mass for the purpose of comparison.

As seen from Table C3, the measured and estimated natural gas fuel mass match well. The natural gas fuel mass is the least for composition 1, due to the maximum amount of hydrogen percentage. The values of natural gas fuel mass for the three tested compositions are lower than the value for ONG performance, which indicates improved engine efficiency. The estimation of engine efficiency for varying fuel compositions has been presented in Section 4. Furthermore, the Seiliger parameters follow expected trends as the tested fuel blends exhibit a higher value of 'a' (more isochoric combustion) compared to ONG performance [58]. Seiliger parameter 'b' decreases (less isobaric combustion) signifying improved combustion stability and combustion rate because of hydrogen. In addition to hydrogen, carbon dioxide can also play a positive role due to the constant NOx operation leading to a counter effect provided by the richening of air–fuel mixture, which can increase the combustion rate and combustion stability [87]. Lastly, the Seiliger parameter 'c' is evidently lower for the hydrogen, carbon dioxide and natural gas fuel blends compared to only natural gas, thus, depicting less late combustion at constant NOx operation. Seiliger parameters 'b' and 'c' are a result of the complex interaction during the combustion process between hydrogen, carbon dioxide, natural gas and air present in the incoming air–fuel charge. In order to capture the in-cylinder process for the anode-off gas and natural gas fuel blends, the above derived Seiliger parameters are used in the Seiliger process model [58]. The simulated in-cylinder pressures and temperatures are compared against engine measurements for the validation of methodology and the parametric equations. Engine performance variables obtained from the Seiliger process model are compared against values obtained from measurements and presented in Table C4 for further validation.

It is evident from Table C4 that the simulated engine performance for the tested AOG-NG fuel blends matches well with the measurements. Therefore, the combination of first-principle Seiliger modelling approach and parametric equations for each anode-off gas constituent are used to

Table C2
Error percentages between the predicted and measured values of performance parameters $20H_2$-NG fuel blend and 500 mg N m^{-3} NOx at 75% load.

Parameter	p_{max}	T_{max}	Work	Q_{net}	p_6	T_6	m_{NG}	UHC
Error [%] ($20H_2$-NG @ 75%)	−0.13	−0.48	−0.94	−0.57	−2.74	−3.18	0.032	1.71
Error [%] ($20CO_2$-NG @ 50%)	−0.64	−0.14	−2.55	−2.46	−5.93	−5.77	0.14	5.71

Table C3
Derived Seilgier parameters and natural gas fuel mass for ONG fuel and the three anode-off gas and natural gas fuel compositions provided in Table 2 at 500 mg N m^{-3} NOx and 75% load.

Composition	a	b	c	$m_{NG,AOG-NG}^{sim}$ [kg]	$m_{NG,AOG-NG}^{meas}$ [kg]
ONG	1.3643	1.452	1.7917	2.9025e-4	2.9029e-4
1	1.4953	1.3517	1.6322	2.6058e-4	2.6465e-4
2	1.4637	1.3658	1.7022	2.6666e-4	2.6818e-4
3	1.4513	1.3945	1.6943	2.7298e-4	2.7877e-4

Table C4
Error percentages between the predicted and measured values of performance parameters for the three anode-off gas and natural gas fuel compositions provided in Table 2 at 500 mg N m^{-3} NOx and 75% load.

Composition	p_{max} [%]	T_{max} [%]	Work [%]	Q_{net} [%]	p_6 [%]	T_6 [%]
1	1.06	1.61	0.94	−0.28	−4.07	−4.42
2	−0.20	0.77	0.54	−0.06	−3.94	−4.2
3	−0.29	1.77	1.48	0.96	−2.6	−2.76

model the in-cylinder process for anode-off gas and natural gas fuel blends. By combining the Seiliger closed-cycle in-cylinder model with an open-cycle mean value model, a holistic engine performance model for AOG-NG fuel blends is employed to study SOFC-ICE integration.

C.3. AOG-NG MVEM description

Fig. C1 shows the schematic representation of the MVEM. The model inputs for the MVEM are load percentage, fuel composition and engine speed. Based on the fuel composition and load setpoint, the model calculates the incoming fuel mass by employing the above derived parametric equations. Similarly, the model estimates the Seiliger parameters, which are used in the Seiliger process model to simulate the in-cylinder process. The in-cylinder process model computes the closed-cycle work ($w_{cycle,seil}$) done per cylinder per unit trapped mass (m_1) by using the Seiliger process. To account for the gas exchange, a defined percentage of the closed-cycle work is assumed to be lost as pumping work loss ($w_{cycle,pump}$). The defined gas exchange percentage is estimated from in-cylinder pressure measurements and derived as a function of engine loading. Closed-cycle work minus the gas exchange gives the indicated work, which on multiplying by firing frequency (f), m_1, generator efficiency (η_{gen}) and mechanical efficiency (η_{mech}) gives the simulated brake power (P_{ICE}). The brake power produced by the engine is estimated from Eq. (C.1).

$$P_{ICE} = m_1.(w_{cycle,seil} - w_{cycle,pump}).f.\eta_{mech}.\eta_{gen} \tag{C.1}$$

The closed-cycle work is a summation of the work during each stage of the Seiliger cycle [58]. The trapped pressure estimation is required to compute the trapped mass, in-cylinder pressures and temperatures, which are used to estimate the closed-cycle work, net combustion heat and brake power. In this research, trapped pressure is assumed to be equal to the manifold pressure after the throttle. The initial value of manifold pressure is derived from fuel flow rate and an initial estimation of air-excess ratio. The fuel flow rate is calculated accurately from the parametric equations discussed in Appendix C.1 and C.2. The parametric equations are also used to calculate the initial value of air-excess ratio for a fixed load percentage and fuel composition as described in Appendix C.1.

Besides work and heat, the Seiliger in-cylinder process model also simulates the exhaust parameters such as temperature, pressure and in-cylinder mass at the point of exhaust valve opening. Since the modelled test engine has a zero valve overlap, the sum of fuel and air mass at trapped condition amount to the total mass exiting the cylinder, however, the composition inside the cylinder changes due to combustion. The change in mass and composition during each Seiliger stage is computed by the mass and composition balance model seen in Fig. C1. Mixture properties such as gas constants and specific heat capacities are calculated as a function of composition and temperature. The exhaust parameters and mixture properties listed in Fig. C1 are used as inputs for the turbocharger and exhaust receiver model. The equations in the turbocharger and exhaust receiver model are based on [2,88,62].

In the AOG-NG MVEM, the effect of two parallel turbochargers, one for each cylinder bank, shown in Fig. A1 is simulated by one large turbocharger for the entire engine. The turbocharger and exhaust receiver model solve for the exhaust temperatures, pressures, charge pressure after the compressor or before the throttle and compressor outlet temperature using the zinner blowdown, Büchi balance and elliptical law.

Based on the above description, the MVEM runs a pre-simulation for an initial estimate of the complete engine performance. The pre-simulation, along with other engine performance variables, gives an estimate of the initial brake-power, which is compared against the input load set-point. The pre-simulation under or overestimates the brake power due to deviations in the estimation of work and initial trapped mass. If the MVEM engine estimates a lower value of brake power then, the manifold pressure (MAP) controller shown in Fig. C1 opens the throttle valve to allow an increased intake of air–fuel charge. The increased air–fuel charge raises the trapped pressure and also increases the brake power. The proportional and integral (PI) manifold pressure controller keeps opening the throttle valve till the estimated brake power matches the required load set-point. In case of a higher initial estimation of the brake power, the PI controller closes the throttle valve till the brake power delivered by the engine reduces and matches the set load point.

For every changing value of MAP until the brake power matches, the MVEM iteratively re-simulates the outputs of the submodels shown in Fig. C1 and, hence, engine performance. These iterative simulations of the MVEM can be understood in the following manner. For every change in value of manifold pressure, a new value of air-excess ratio is computed, considering the fuel mass estimation based on the parametric equation to be accurate and fixed. At each step, the changing MAP changes the trapped mass, trapped temperature, air-excess ratio, mass balance, composition balance, in-cylinder pressures, temperatures, turbocharger performance and emissions. The final and corrected values of manifold pressure and air-excess ratio correspond to the iteration for which simulated brake-power is equal to the required load. The MVEM re-simulates the engine performance for this final iteration based on the final value of MAP and air-excess ratio by solving the equations for the Seiliger in-cylinder process model, mass and composition balance model and the turbocharger plus exhaust receiver model. Furthermore, the new and final air-excess ratio value is also used to calculate the final values of engine exhaust emissions of NOx, CO_2 and UHC in g kW^{-1} h^{-1}. The equations for calculating the engine exhaust emissions in are based on [89]. The UHC emissions are first calculated in ppmv by using the earlier derived parametric equations and then converted to g kW^{-1} h^{-1}. In addition to the engine emissions, engine efficiency is also calculated as model output by using Eq. (C.2).

$$\eta_{ICE} = \frac{P_{ICE}}{\dot{m}_{fuel}.LHV_{fuel}} \tag{C.2}$$

where 'P_{ICE}' is the brake engine power in kW. '$\dot{m}_{fuel}$' is the total fuel flow rate in kg s^{-1} and 'LHV' is the lower heating value of the fuel calculated in kJ kg^{-1}. Fuel properties such as stoichiometric air–fuel ratio, density and lower heating value for the engine model are based on fuel composition and vary with changing percentages of hydrogen, carbon dioxide and natural gas in the fuel.

Appendix D. Example efficiency calculation for SOFC-ICE integration

In this appendix, an example calculation for the efficiency of the integration SOFC-ICE system has been presented. The efficiency has been calculated for a 50–50 SOFC-ICE power split with a total power output of 750 kWe. The SOFC operates at a current density of 4750 A m^{-2}, fuel utilization of 80% and pre-reforming of 0.3. The total numbers of cells is fixed at 11000. The integrated ICE operates on a 30–70 AOG-NG fuel

comprising of 12.81% hydrogen and 17.19% carbon dioxide, by volume. This operating condition corresponds to the condition depicted with a vertical dashed line in Fig. 7. The following steps are followed to calculate the system efficiency:

Step 1: The efficiency of the SOFC is calculated by using Eq. (D.1)

$$\eta_{SOFC} = \frac{P_{SOFC,AC}}{\dot{N}^{in}_{CH4}.LHV_{CH4}} \tag{D.1}$$

where '$P_{SOFC,AC}$' is the AC stack power simulated by the model for the given operating conditions, which is equal to 373.8259 kWe. '$\dot{N}^{in}_{CH4}$' is the total molar flow rate of methane corresponding to the total number of cells, which is equal to 0.8448 mol s^{-1}. 'LHV_{CH4}' is the lower heating value of CH_4, which is equal to 802.6×10^3 kJ mol^{-1}. Using these values, the efficiency of the SOFC is calculated to be 55.14%.

Step 2: The efficiency of the integrated ICE is calculated by the AOG-NG model using Eq. (D.2).

$$\eta_{I-ICE} = \frac{P_{ICE}}{\dot{m}_{fuel}.LHV_{fuel} - \dot{m}_{H_2}.LHV_{H_2}} \tag{D.2}$$

where 'P_{ICE}' is the brake power output of the ICE, which was 376.17 kWe. '$\dot{m}_{fuel}$' is the total AOG-NG fuel flow rate entering the ICE, which is equal to 152.026 kg h^{-1} or 0.0422 kg s^{-1} for the given operating conditions. '$\dot{m}_{H_2}$' is the flow rate of hydrogen from the SOFC used in the 30–70 AOG-NG blend consumed in the ICE, which is equal to 1.6253 kg h^{-1} or 4.5896×10^{-4} kg s^{-1}. 'LHV_{fuel}' and 'LHV_{H_2}' are equal to 26.01 MJ kg^{-1} and 127.53 MJ kg^{-1}, which are the lower heating values of the 30–70 AOG-NG blend and hydrogen, respectively, calculated by the AOG-NG MVEM. Using these values and Eq. (D.2), the efficiency of the integrated engine was calculated to be 36.24%. This efficiency value corresponds to the efficiency of the integrated ICE, which excludes the incoming energy contribution of hydrogen since it is obtained from the SOFC and, thus, accounted for in the SOFC efficiency calculation. If the incoming energy of hydrogen is taken into account in the efficiency calculation, then the efficiency of the standalone ICE operating on the same 30–70 AOG-NG blend is 34.27%. Therefore, the efficiency of the integrated AOG-NG ICE is higher than that of the standalone ICE operating on the same 30–70 AOG-NG blend by about 2%. At the same time, the efficiency of the integrated AOG-NG ICE is higher than that of the standalone ICE operating on only NG at 375 kWe by about 2.56%. Thus, hydrogen addition from AOG caused a 0.6% efficiency improvement solely due to better combustion.

Step 3: Based on the estimated efficiencies of the SOFC and integrated AOG-NG ICE, the efficiency of the SOFC-ICE system is calculated by applying Eq. (D.3).

$$\eta_{SOFC-ICE} = \frac{P_{SOFC-ICE}}{EC_{SOFC} + EC_{I-ICE}} \tag{D.3}$$

where '$P_{SOFC-ICE}$' is the total power output of the system, which is equal to 750 kWe. 'EC_{SOFC}' represents the incoming energy contribution of the SOFC while 'EC_{I-ICE}' represents the incoming energy contribution of the integrated engine. These two values are calculated by dividing the individual power outputs of each component by its corresponding efficiency computed using Eqs. (D.1) and (D.2). In this manner, EC_{SOFC} was computed to be 678.036 kW while EC_{I-ICE} was computed to be 1039.8705 kW. Based on these values the efficiency of the integrated SOFC-ICE system for the given operating conditions is estimated to be 43.657%, which can be seen in Fig. 7.

Appendix E. Verification of SOFC transients

The 0-D model input parameters for the dynamic load response simulations are as follows [33,76]. Fuel and air inlet temperatures are kept at 1023 K. The operating pressure is ambient (100 kPa); initial current density in the 0-D model is maintained at 5000 A m^{-2}; fuel utilization is constant at 75% and air-excess ratio is constant at 8.5. The incoming composition for the anode-flow channel is obtained as a result of 10% pre-reforming with S/C ratio of 2. To verify the dynamic simulation capabilities of the 0-D SOFC model, the 0-D model is tested for a +2000 A m^{-2} current density ramp in 60 s [33,76]. In this simulation study, the ramp is introduced after the model reaches steady state conditions for 5000 A m^{-2} current density. After reaching steady state, the model simulates the load response for change in current density from 5000 A m^{-2} to 7000 A m^{-2}.

Fig. E1 depicts the verification of the dynamic capabilities of the 0-D model by comparing the normalized cell voltage and PEN temperature against the results reported by the reference publication of Salogni et al. [33] for the same test conditions. As seen from the figure, the qualitative trends of voltage and temperature simulated by the 0-D model match well with that of the reference. The absolute values of PEN temperature simulated by the 0-D model are quite close to the values obtained from the reference 1-D model. Both the models show a drop (undershoot) in cell voltage followed by a settling period due to the ramp in current density while the PEN temperature increases. As the current density is increased, the ohmic and activation losses increase causing the cell voltage to drop. At the same time, the fuel flow increases to maintain the same fuel utilization, thus, resulting in higher PEN temperatures due to the increased heat release during the hydrogen oxidation of more incoming hydrogen at higher current densities. However, there is a lag in temperature response compared to the chemical kinetics, which leads to larger voltage losses and an undershoot in cell voltage due to lower temperatures. As the PEN temperature increases and settles, the cell voltage also progresses through a settling period and reaches steady state. Both the models depict very similar settling periods and time scales for reaching steady state.

Although the overall dynamic response simulated by the 0-D model qualitatively matches well with the reference, a few differences can be noted in simulation results. The 1-D reference model depicts a larger voltage drop. Furthermore, the 1-D model from the reference shows an initial drop in PEN temperature, which significantly contributes to the lag and, hence, the large voltage drop as seen in Fig. E1. This initial drop in PEN temperature was simulated by the 1-D model at the exhaust discharge section [33] and could be attributed to a different control strategy or setting, which caused a sudden increase in air-intake to maintain the same air-excess ratio of 8.5. This drop in PEN temperature at the exhaust discharge section is not simulated by the 0-D SOFC model. A 1-D model is recommended to more accurately simulate the temperature variations and the voltage response while accounting for maximum thermal gradients and stresses encountered during SOFC dynamics.

It is clear from the above discussion that although the 0-D model found some differences in simulating the quantitative voltage and temperature dynamics, it was successful in capturing the time scales of a SOFC load response.
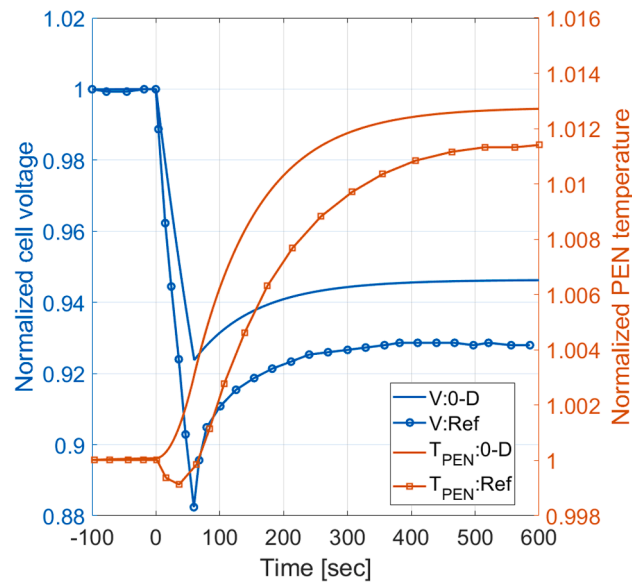
Fig. E1. 0-D SOFC model verification in simulating dynamic response. Normalized SOFC voltage and PEN temperature response for change in current density from 5000 to 7000 A m^{-2}. The simulation output of the 0-D SOFC model is compared against results reported in [33].

References

[1] Sun Y, Wang H, Yang C, Wang Y. Development and validation of a marine sequential turbocharging diesel engine combustion model based on double Wiebe function and partial least squares method. Energy Convers Manage Nov 2017;151: 481–95.

[2] Geertsma RD, Negenborn RR, Visser K, Loonstijn MA, Hopman JJ. Pitch control for ships with diesel mechanical and hybrid propulsion: Modelling, validation and performance quantification. Appl Energy 2017;206:1609–31.

[3] Reduction of GHG emissions from ships - Third IMO GHG Study 2014 - Final Report, Tech. rep., IMO, 2014.

[4] MARPOL ANNEX VI and NTC 2008 with guidelines for implementation - supplement, Tech. Rep. September 2015, IMO, 2015.

[5] Van Biert L, Godjevac M, Visser K, Aravind P. A review of fuel cell systems for maritime applications. J Power Sources 2016;327:345–64.

[6] Verbeek R, Bolech M, den Uil H. Alternative fuels for sea shipping, Tech. rep., 2011.

[7] Aceves SM, Espinosa-Loza F, Ledesma-Orozco E, Ross TO, Weisberg AH, Brunner TC, et al. High-density automotive hydrogen storage with cryogenic capable pressure vessels. Int J Hydrogen Energy Feb 2010;35:1219–26.

[8] Fuel Oil - Storage Tanks. www.engineeringtoolbox.com/fuel-oil-storage -tanks-dimensions-d_1585.html.

[9] LNG Storage Vessels. www.ChartLNG.com, 2016.

[10] Metkemeijer R, Achard P. Comparison of ammonia and methanol applied indirectly in a hydrogen fuel cell. Int J Hydrogen Energy 1994;19(6):535–42.

[11] OECD-FAO Agricultural Outlook 2018–2027, Tech. rep., OECD and Food and Agriculture Organization of the United Nations, 2018.

[12] Oil - World Energy Outlook 2018. www.iea.org/reports/w orld-energy-outlook-2018/oil#abstract.

[13] Gas - World Energy Outlook 2019. www.iea.org/reports/w orld-energy-outlook-2019/gas#abstract.

[14] Satyapal S. Hydrogen and Fuel Cells Overview, Tech. rep., US Department of Energy, 2019.

[15] Nitrogen (Fixed)-Ammonia, Tech. rep., U.S. Geological Survey, 2018.

[16] Global average bunker price. www.shipandbunker. com/prices/av/global/av-glb-global-average-bunker-price#MGO.

[17] Clean Cities Alternative Fuel Price Report, April 2019, Tech. rep., U.S. Department of Energy, 2019.

[18] Widmar D. Nitrogen leads fall 2019 fertilizer prices lower. www.aei.ag/2019/10/ 14/nitrogen-leads-fall-2019-fertilizer-prices-lower, 2019.

[19] Market price: Dimethyl ether. www.ceicdata.com/en/china/china-petroleum-c hemical-industry-association-petrochemical-price-organic-chemical-mater ial/cn-market-price-monthly-avg-organic-chemical-material-dimethyl-ether- 990-or-above.

[20] Methanex monthly average regional posted contract price history, Tech. rep., Methanex, 2017.

[21] Connelly E, Penev M, Elgowainy A, Hunter C. Current status of hydrogen liquefaction costs. tech. rep. USA: Department of Enerrgy; 2019.

[22] Maritime Assessment of Selected Alternative Fuels and Technologies, Tech. rep., DNVGL, 2019.

[23] Ramadhani F, Hussain MA, Mokhlis H. A comprehensive review and technical guideline for optimal design and operations of fuel cell-based cogeneration systems. Processes 2019.

[24] McPhail SJ, Aarva A, Devianto H, Bove R, Moreno A. SOFC and MCFC: Commonalities and opportunities for integrated research. Int J Hydrogen Energy 2011;36:10337–45.

[25] Baldi F, Wang L, Pérez-Fortes M, Maréchal F. A cogeneration system based on solid oxide and proton exchange membrane fuel cells with hybrid storage for off-grid applications. Front Energy Res Jan 2019;6:139.

[26] Zhang X, Chan SH, Li G, Ho HK, Li J, Feng Z. A review of integration strategies for solid oxide fuel cells. J Power Sources Feb 2010;195:685–702.

[27] Buonomano A, Calise F, D`Accadia MD, Palombo A, Vicidomini M. Hybrid solid oxide fuel cells-gas turbine systems for combined heat and power: A review. Appl Energy Oct 2015;156:32–85.

[28] Van Biert L, Woudstra T, Godjevac M, Visser K, Aravind P. A thermodynamic comparison of solid oxide fuel cell-combined cycles. J Power Sources 2018;397: 382–96.

[29] Chan SH, Ho HK, Tian Y. "Modelling of simple hybrid solid oxide fuel cell and gas turbine power plant. J Power Sources 2002;109:111–20.

[30] Park SK, Kim TS. Comparison between pressurized design and ambient pressure design of hybrid solid oxide fuel cell-gas turbine systems. J Power Sources 2006; 163:490–9.

[31] Chuahy FDF, Kokjohn SL. Solid oxide fuel cell and advanced combustion engine combined cycle: A pathway to 70% electrical efficiency. Appl Energy Feb 2019; 235:391–408.

[32] Chan SH, Ho HK, Tian Y. Modelling for part-load operation of solid oxide fuel cell-gas turbine hybrid power plant. J Power Sources Mar 2003;114:213–27.

[33] Salogni A, Colonna P. Modeling of solid oxide fuel cells for dynamic simulations of integrated systems. Appl Therm Eng 2010;30(5):464–77.

[34] Wartsila. Combustion Engine vs. Gas Turbine-Part Load Efficiency and Flexibility. https://www.wartsila.com/energy/learn-more/technical-comparisons/combus tion-engine-vs-gas-turbine-part-load-efficiency-and-flexibility.

[35] Wartsila. Combustion Engine vs Gas Turbine-Startup time. https://www.wartsila. com/energy/learn-more/technical-comparisons/combustion-engine-vs-gas-turbin e-startup-time.

[36] Campanari S, Mastropasqua L, Gazzani M, Chiesa P, Romano MC. Predicting the ultimate potential of natural gas SOFC power cycles with CO2 capture - Part A: Methodology and reference cases. J Power Sources Aug 2016;324:598–614.

[37] Park SH, Lee YD, Ahn KY. Performance analysis of an SOFC/HCCI engine hybrid system: System simulation and thermo-economic comparison. Int J Hydrogen Energy 2014;39(4):1799–810.

[38] Lee YD, Ahn KY, Morosuk T, Tsatsaronis G. Exergetic and exergoeconomic evaluation of an SOFC-Engine hybrid power generation system. Energy Feb 2018; 145:810–22.

[39] Edwards C, Fyffe J, Donohue M, Regalbuto C. Exploration of a Fuel fell/Internal combustion engine combined cycle for high efficiency power generation (A GCEP exploratory project), 2013.

[40] Kim J, Kim Y, Choi W, Ahn KY, Song HH. Analysis on the operating performance of 5-kW class solid oxide fuel cell-internal combustion engine hybrid system using spark-assisted ignition. Appl Energy Feb 2020;260:114231.

[41] Zhu P, Yao J, Qian C, Yang F, Porpatham E, Zhang Z, et al. High-efficiency conversion of natural gas fuel to power by an integrated system of SOFC, HCCI

engine, and waste heat recovery: Thermodynamic and thermo-economic analyses. Fuel 2020;275:117883.

[42] Choi W, Kim J, Kim Y, Kim S, Oh S, Song HH. Experimental study of homogeneous charge compression ignition engine operation fuelled by emulated solid oxide fuel cell anode off-gas. Appl Energy Nov 2018;229:42–62.

[43] Choi W, Song HH. Composition-considered Woschni heat transfer correlation: Findings from the analysis of over-expected engine heat losses in a solid oxide fuel cell-internal combustion engine hybrid system. Energy Jul 2020;203:117851.

[44] Bessonette PW, Schleyer CH, Duffy KP, Hardy WL, Liechty MP. Effects of fuel property changes on heavy-duty hcci combustion. In: SAE Technical Paper, SAE International; 2007.

[45] Dec JE, Yang Y, Dronniou N. Boosted hcci-controlling pressure-rise rates for performance improvements using partial fuel stratification with conventional gasoline. SAE Int J Engines 2011;4(1):1169–89.

[46] Kokjohn SL, Hanson RM, Splitter DA, Reitz RD. Experiments and modeling of dual-fuel hcci and pcci combustion using in-cylinder fuel blending. SAE Int J Engines 2010;2(2):24–39.

[47] Choi W, Kim J, Kim Y, Song HH. Solid oxide fuel cell operation in a solid oxide fuel cell-internal combustion engine hybrid system and the design point performance of the hybrid system. Appl Energy Nov 2019;254:113681.

[48] Wu Z, Tan P, Zhu P, Cai W, Chen B, Yang F, et al. Performance analysis of a novel SOFC-HCCI engine hybrid system coupled with metal hydride reactor for H2 addition by waste heat recovery. Energy Convers Manage Jul 2019;191:119–31.

[49] Chaudhari VD, Deshmukh D. Challenges in charge preparation and combustion in homogeneous charge compression ignition engines with biodiesel: A review. Energy Rep Nov 2019;5:960–8.

[50] Ran Z, Assanis D, Hariharan D, Mamalis S. Experimental study of spark-ignition combustion using the anode off-gas from a solid oxide fuel cell. SAE Technical Papers, vol. 2020-April, 2020, p. 1–8.

[51] Welaya YM, Mosleh M, Ammar NR. Energy analysis of a combined solid oxide fuel cell with a steam turbine power plant for marine applications. J Marine Sci Appl 2014;65(1):97–116.

[52] Kang S, Ahn K-Y. Dynamic modeling of solid oxide fuel cell and engine hybrid system for distributed power generation. Appl Energy 2017;195:1086–99.

[53] Hartman J. Turbocharging performance handbook, 2007.

[54] Theotokatos GP. A modelling approach for the overall ship propulsion plant simulation. In: 8th WSEAS conference on system science and simulation in engineering, vol. 2, 2007, p. 80–7.

[55] Taskar B, Yum KK, Steen S, Pedersen E. The effect of waves on engine-propeller dynamics and propulsion performance of ships. Ocean Eng Aug 2016;122:262–77.

[56] Reitz RD, Duraisamy G. Review of high efficiency and clean reactivity controlled compression ignition (RCCI) combustion in internal combustion engines. Prog Energy Combust Sci Feb 2015;46:12–71.

[57] Aguiar P, Adjiman CS, Brandon NP. Anode-supported intermediate temperature direct internal reforming solid oxide fuel cell. I: Model-based steady-state performance. J Power Sources 2004;138(1–2):120–36.

[58] Sapra H, Godjevac M, Vos PD, Sluijs WV, Linden Y, Visser K. Hydrogen-natural gas combustion in a marine lean-burn, SI engine: A comparitive analysis of Seiliger and double Wiebe function-based zero-dimensional modelling. Energy Convers Manage 2020:1–32.

[59] Marra D, Pianese C, Polverino P, Sorrentino M. Models for solid oxide fuel cell systems exploitation of models hierarchy for industrial design of control and diagnosis strategies, Tech. rep., 2016.

[60] Van Biert L, Godjevac M, Visser K, Aravind PV. Dynamic modelling of a direct internal reforming solid oxide fuel cell stack based on single cell experiments. J Appl Energy 2019.

[61] Van Biert L, Visser K, Aravind PV. "Intrinsic methane steam reforming kinetics on nickel-ceria solid oxide fuel cell anodes. J Power Sources 2019;443:227261.

[62] Reurings JW. A modeling study to investigate performance of SOFC-ICE hybrid systems for marine applications. Master's thesis, Delft University of Technology. 2019.

[63] Larminie J, Dicks A. Fuel cell systems explained. second ed., 2003.

[64] Weinberg FJ. Explicit equations for the calculation, by successive approximations, of equilibrium gas compositions at high temperatures: The hydrogen+carbon+

[65] oxygen and the hydrogen+carbon+oxygen+nitrogen systems without solid carbon formation, 1957.

[66] Perry S, Perry RH, Green DW, Maloney JO. Perry's chemical engineers' handbook, vol. 38, 2000.

[67] Noren DA, Hoffman MA. Clarifying the Butler-Volmer equation and related approximations for calculating activation losses in solid oxide fuel cell models. J Power Sources Dec 2005;152:175–81.

[68] Fang Q, Blum L, Peters R, Peksen M, Batfalsky P, Stolten D. SOFC stack performance under high fuel utilization. Int J Hydrogen Energy Jan 2015;40:1128–36.

[68] Arruga H, Scholl F, Kettner M, Amad OI, Klaissle M, Giménez B. Effect of intake manifold water injection on a natural gas spark ignition engine: an experimental study. In: IOP Conference Series: Materials Science and Engineering; 2017.

[69] Khan MZ, Song RH, Hussain A, Lee SB, Lim TH, Hong JE. Effect of applied current density on the degradation behavior of anode-supported flat-tubular solid oxide fuel cells. J Eur Ceram Soc Apr 2020;40:1407–17.

[70] CIMAC Working Group 17: Gas Engines. Methane and Formaldehyde Emissions of Gas Engines, vol. 17, 2014.

[71] 10 Noteworthy LNG-Powered Vessels. https://www.marineinsight.com/tech/10-noteworthy-lng-fueled-vessels/.

[72] Energy Server ES5-300kW Data Sheet — Bloom Energy. www.bloomenergy.com/datasheets/energy-server-es5-300kw.

[73] Products - Convion. http://convion.fi/products/.

[74] Sunfire Home: Power Plant for your Home - Sunfire. https://www.sunfire.de/en/products-and-technology/sunfire-home.

[75] CAT CG132B-8 — 280kW-400kW Gas Generator. www.cat.com/en_US/products/new/power-systems/electric-power/gas-generator-sets/2841734473578834.html.

[76] Iora P, Aguiar P, Adjiman CS, Brandon NP. "Comparison of two IT DIR-SOFC models: Impact of variable thermodynamic, physical, and flow properties. Steady-state and dynamic analysis," jun. Chem Eng Sci 2005;60:2963–75.

[77] Technical documentation, Integrated Stack Module (ISM), Tech. rep., Staxera, 2010.

[78] Andrea GD, Gandiglio M, Lanzini A, Santarelli M. Dynamic model with experimental validation of a biogas-fed SOFC plant. Energy Convers Manage 2017;135:21–34.

[79] CIMAC WG17 'Gas Engines'. Transient response behaviour of gas engines. Position Paper of the International Concil on Combustion Engines (CIMAC), 2011, p. 1–7.

[80] Packham K. Lean-burn engine technology increases efficiency, reduces NOx emissions (White paper). 2007.

[81] KiBox To Go — Kistler. www.kistler.com/en/products/systems/kibox-to-go/.

[82] Azzopardi M. Dynamic modelling implementation for a multi-purpose 1-D planar SOFC: Gaining insight behaviour into an intermediate temperature SOFC, Master's thesis, Delft University of Technology, 2017.

[83] Papurello D, Lanzini A, Fiorilli S, Smeacetto F, Singh R, Santarelli M. Sulfur poisoning in Ni-anode solid oxide fuel cells (SOFCs): Deactivation in single cells and a stack. Chem Eng J Jan 2016;283:1224–33.

[84] de Wild PJ, Nyqvist RG, de Bruijn FA, Stobbe ER. Removal of sulphur-containing odorants from fuel gases for fuel cell-based combined heat and power applications. J Power Sources 2006;159:995–1004.

[85] Matsuzaki Y, Yasuda I. Electrochemical oxidation of H2 and CO in a H2–H2O-CO-CO2 system at the interface of a Ni-YSZ cermet electrode and YSZ electrolyte. J Electrochem Soc May 2000;147:1630–5.

[86] Waldheim T, Nilsson L. Heating value of gases from biomass gasification. IEA Bioenergy Agreement, Task 20 - Thermal Gasification of Biomass, 2001, p. 61.

[87] Bauer M, Muenchen TU. Formation of formaldehyde in lean burn gas engines, 2009.

[88] Stapersma D. Diesel engines: A fundamental approach to performance analysis, turbocharging, combustion, emissions and heat transfer including thermodynamical principles. vol. 2: Turbocharging, 2010.

[89] Stapersma D. Diesel engines: A fundamental approach to performance analysis, turbocharging, combustion, emissions and heat transfer including thermodynamical principles. vol. 4: Emissions and Heat Transfer, vol. 4. 2010.